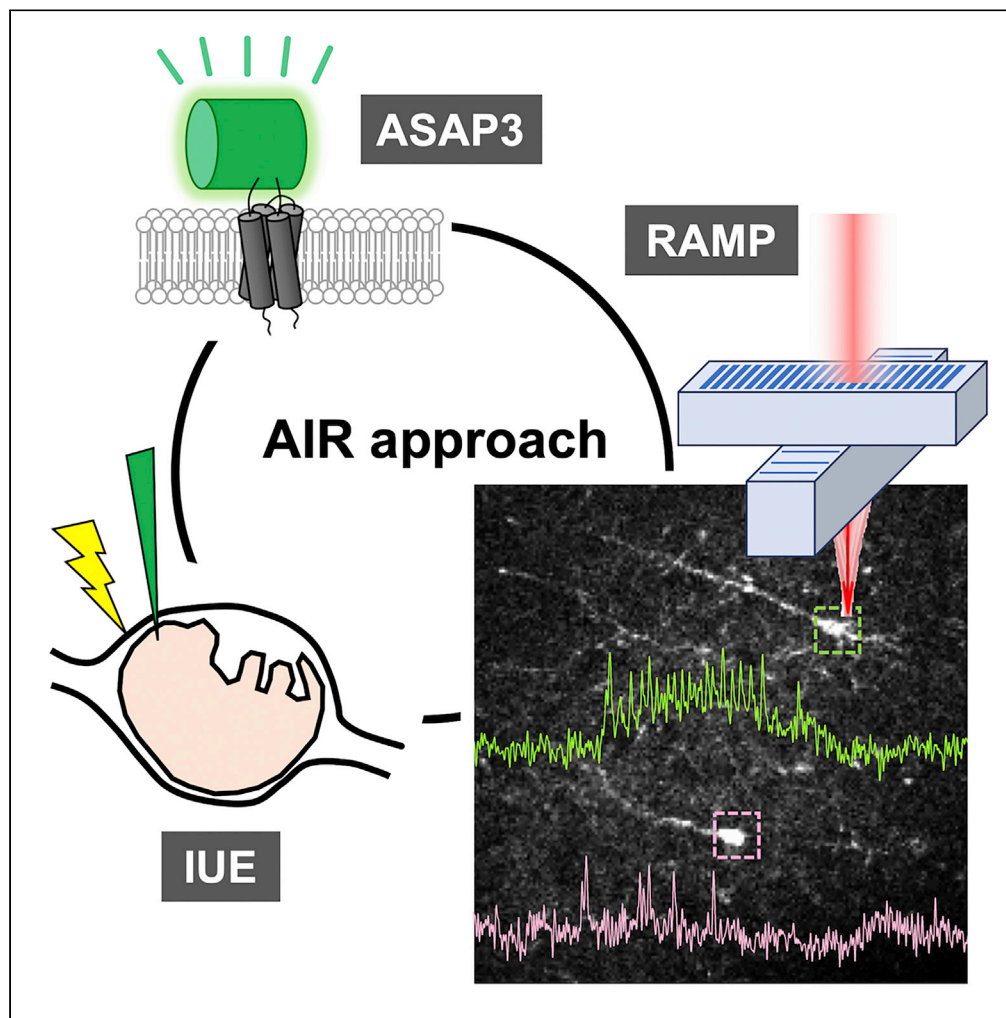


## Article

## Two-Photon Voltage Imaging of Spontaneous Activity from Multiple Neurons Reveals Network Activity in Brain Tissue



Binglun Li, Mariya Chavarha, Yuho Kobayashi, Satoshi Yoshinaga, Kazunori Nakajima, Michael Z. Lin, Takafumi Inoue

inoue.t@waseda.jp

**HIGHLIGHTS**

Kilohertz-order two-photon voltage imaging with single-trial acquisition

Readout spontaneous activity from multi-cells or subcellular regions simultaneously

Long-duration voltage imaging insuring functional studies of neuron circuit

Functional connections analysis with greater precision than calcium imaging

Li et al., iScience 23, 101363  
July 24, 2020 © 2020 The Author(s).  
<https://doi.org/10.1016/j.isci.2020.101363>

## Article

## Two-Photon Voltage Imaging of Spontaneous Activity from Multiple Neurons Reveals Network Activity in Brain Tissue

Binglun Li,<sup>1</sup> Mariya Chavarha,<sup>2</sup> Yuho Kobayashi,<sup>1</sup> Satoshi Yoshinaga,<sup>3</sup> Kazunori Nakajima,<sup>3</sup> Michael Z. Lin,<sup>2</sup> and Takafumi Inoue<sup>1,4,\*</sup>

## SUMMARY

**Recording the electrical activity of multiple neurons simultaneously would greatly facilitate studies on the function of neuronal circuits. The combination of the fast scanning by random-access multiphoton microscopy (RAMP) and the latest two-photon-compatible high-performance fluorescent genetically encoded voltage indicators (GEVIs) has enabled action potential detection in deep layers in *in vivo* brain. However, neuron connectivity analysis on optically recorded action potentials from multiple neurons in brain tissue has yet to be achieved. With high expression of a two-photon-compatible GEVI, ASAP3, via *in utero* electroporation and RAMP, we achieved voltage recording of spontaneous activities from multiple neurons in brain slice. We provide evidence for the developmental changes in intralaminar horizontal connections in somatosensory cortex layer 2/3 with a greater sensitivity than calcium imaging. This method thus enables investigation of neuronal network connectivity at the cellular resolution in brain tissue.**

## INTRODUCTION

Precise recording of activities of multiple neurons is critical for understanding how the activity of neuronal circuits represents and processes information, and thereby underlies the brain function. Among the complex neural activities, synchronous firing is commonly observed in many brain areas (Stern et al., 1998; Usrey and Reid, 1999). It is the most basic temporal relationship among neurons in the network (deCharms and Zador, 2000) and plays a crucial role in encoding and decoding of neuronal language (Jadhav et al., 2009; Mizuno et al., 2018; Xu et al., 2011). According to Hebb's theory stating that cells that fire together wire together (Hebb, 2005), synchronous firing can be a clue to the functional connection of the underlying network. Multi-electrode array (Diba et al., 2014), multiple patch clamp (Han et al., 2018; Jouhanneau et al., 2018), and calcium imaging (Golshani et al., 2009; Sadakane et al., 2015) have been applied to investigate functional connectivity of neurons in circuits by recording activities of multiple neurons simultaneously. Although the electrophysiological measurements are superior in temporal resolution, they are invasive and laborious. Calcium imaging offers easier and less invasive recording with better spatial resolution (Grienberger and Konnerth, 2012; Peterka et al., 2011), but intracellular  $\text{Ca}^{2+}$  concentration is only a proxy of electrical activity and the kinetics of  $\text{Ca}^{2+}$  change is too slow to follow precise action potentials.

Voltage imaging is an alternative approach that directly reports membrane potential changes by action potentials and subthreshold activities. Benefiting from its higher throughput than electrophysiological approaches and the better temporal resolution than calcium imaging, voltage imaging offers a possibility to answer open questions such as how information is processed and propagated in neural circuits. Both chemical and genetically encoded-fluorescent voltage indicators have undergone major development in the past several years. Now they have reached 30%–40% signal change per action potential with millisecond-order kinetics, enabling single-trial action potential detection (Abdelfattah et al., 2019; Adam et al., 2019; Bayguinov et al., 2017; St-Pierre et al., 2014). Compatibility with two-photon microscopy has been highly demanded for monitoring neuron activities deep in brain tissue with better spatial resolution, lower background fluorescence, and lower phototoxicity (Svoboda and Yasuda, 2006). Although chemical voltage sensors have achieved two-photon compatibility together with high dynamic range and fast kinetics earlier than genetically encoded voltage indicators (GEVIs) (Fink et al., 2012; Kuhn et al., 2008; Kulkarni and Miller, 2017), two-photon-compatible GEVIs were awaited, which offer much

<sup>1</sup>Department of Life Science and Medical Bioscience, School of Advanced Science and Engineering, Waseda University, Tokyo 162-8480, Japan

<sup>2</sup>Department of Neurobiology, School of Medicine, Stanford University, Stanford, CA 94305-5090, USA

<sup>3</sup>Department of Anatomy, Keio University School of Medicine, Tokyo 160-8582, Japan

<sup>4</sup>Lead Contact

\*Correspondence: inoue.t@waseda.jp

<https://doi.org/10.1016/j.isci.2020.101363>



easier and non-invasive labeling in tissue with cell-type selectivity. A GEVI, ASAP3, was developed fulfilling the requirements, strong brightness, high sensitivity, and fast kinetics under two-photon illumination (Villette et al., 2019).

Combining the fast scanning by acousto-optic deflectors with the deep tissue penetration property of two-photon microscopy, random-access multiphoton microscopy (RAMP) has potential to detect action potentials in multiple neurons in brain tissue with more than 20 kHz frame rate (Iyer et al., 2006; Salomé et al., 2006). Villette et al. developed the ULoVE method based on RAMP, which enables stable action potential detection in the 3D space in *in vivo* preparation (Villette et al., 2019). However, recording action potentials optically from multiple neurons in brain tissue for neuron connectivity analysis has yet to be achieved.

Functional connection in somatosensory cortex layer (L) 2/3 has been revealed (Thomson, 2007), and conflicting observations on its developmental changes have been raised. Studies using electrophysiology (Holmgren et al., 2003), photostimulation (Boucsein et al., 2011), and calcium imaging (Cheng et al., 2011) demonstrated a negative association between horizontal distance of neuron pair and their connection strength in somatosensory cortex L2/3 in adult mice, whereas another study reported that network activity in this area was highly correlated and the correlation was negatively associated with neuron distance during the first postnatal week, and the correlation disappeared after the second postnatal week (Golshani et al., 2009). In this study, we monitored spontaneous neuronal activities from multiple neurons in somatosensory cortex L2/3 in slice preparation using ASAP3 and RAMP. After characterization and validation of the system, we investigated postnatal changes in functional connectivity with a Jitter-based correlation analysis method (Agmon, 2012). Our results provide a solution to the controversy. We thereby propose that the method developed in this study can be a clue to the functional analysis of neural circuits.

## RESULTS

### Detection of Spontaneous Action Potentials with RAMP Voltage Imaging in Acute Slice

We adopted IUE as a gene delivery method (Tabata and Nakajima, 2008), resulting in strong and sparse ASAP3 expression in specific layers in cerebral cortex in acute slice preparations (Figures 1A and 1B). We recorded spontaneous neuronal activity using a RAMP microscope from neurons with high ASAP3 expression levels by setting single recording voxel on the cell somata at a sampling frequency of 2 kHz (Figures 1C and 1D). Large (>10%) and rapid AP-like fluorescence spikes were observed in one neuron (Figure 1C, pink), whereas a different nearby neuron was silent over the course of the recording (green). By obtaining similar records repeatedly (three more examples in Figure S1), we considered that the optical spikes were not due to noise of the system. This method, combination of ASAP3 of high sensitivity, IUE of strong and sparse expression, and RAMP of fast sampling rate, termed as AIR, enabled optical readout of electrical activities of multiple neurons in single trial.

### Effect of Noise Filter

Faithful detection of neuronal activities with AIR high signal to noise ratio (SNR) is crucial; therefore, we examined low-pass filter parameters as an effective way to reduce noise. A fluorescence trace containing 14 regular fAPs was filtered with Butterworth low-pass filters cutting off at 6–400 Hz (Figure 2A). The signal level ( $-\Delta F/F$ ) was linearly fitted with the common logarithm of filter frequency ( $-\Delta F/F = B + A \times \log_{10}(v)$ , A and B are constants,  $v$  corresponds to frequency; Figure 2B), and the noise level was well fitted with  $\log_{10}(v)$  by a power law ( $N/F = B + A \times \log_{10}(v)^{pow}$ ; Figure 2C). The determined power of  $0.502 \approx 0.5$  is well in agreement with a prediction (Quicke et al., 2019). The relationship between SNR and the filter cutoff frequency showed that optimal filtering should occur at 37 Hz to gain the largest SNR for this particular optical recording condition (Figure 2D). We evaluated the optimal filter cutoff frequencies in fluorescence traces showing variety of firing patterns, e.g., regular (Figure 2) and burst (Figure S2) firing patterns, obtaining  $50.8 \pm 13.1$  Hz (mean  $\pm$  standard deviation [SD],  $n = 6$  neurons) as the mean optimal filter frequency. With this cutoff filter frequency, 14 and 21 fAPs were detected from the traces shown in Figures 2A and S2A, respectively, whereas 0 and 2 fAPs without filter (gray traces) with the same spike detection method (see Transparent Methods).

Cutoff frequency also influences the temporal resolution of optical records. We used spike timing accuracy as an index to evaluate the temporal resolution (see Transparent Methods and Figure S3). Cutoff at 50 Hz resulted in a millisecond-order spike-timing accuracy. Difference in spike timing in traces recorded from two different locations of the same cell body was 1.6 ms (interquartile ranges [IQRs], 1, 2.8; SD = 2.26) (Figures

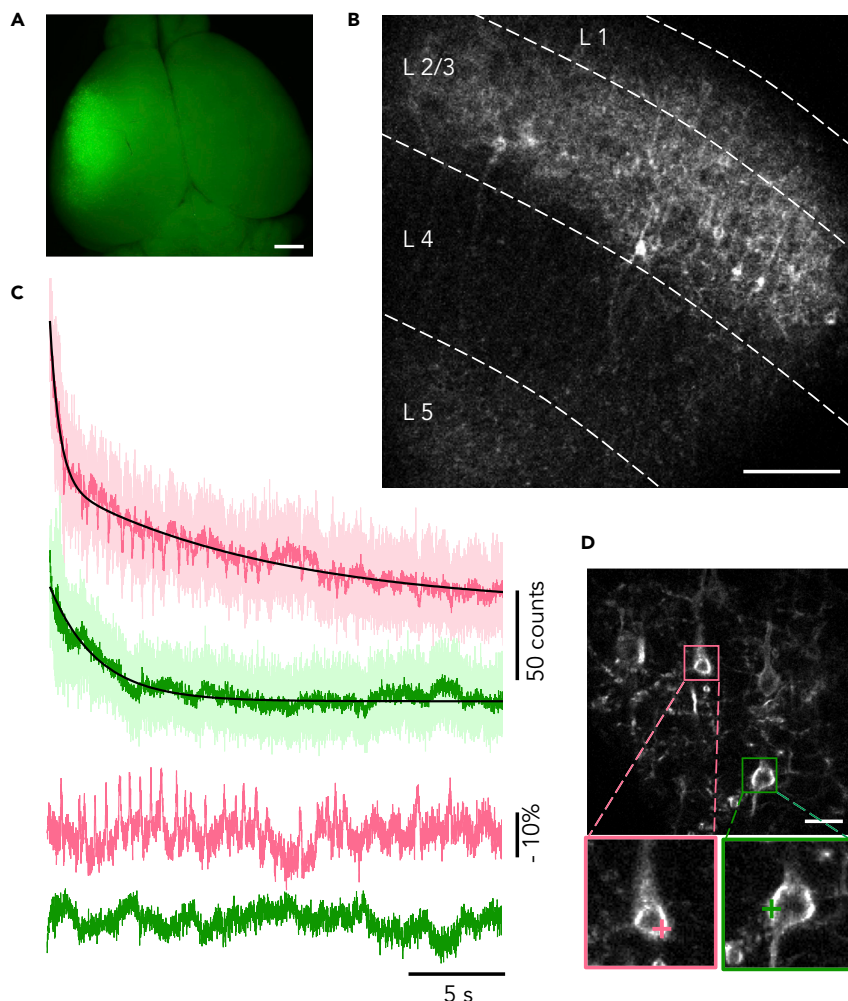


**Figure 1. Expression of ASAP3 in Murine Somatosensory Cortex via IUE and Membrane Potential Recording with Random-Access, Single-Trial, and Single-Voxel Two-Photon Voltage Recording from Multiple Sites in Acute Slice**

(A) Mouse brain at P8 after electroporation of pCAG-ASAP3b at E15.5.

(B) Representative two-photon single-plane image of ASAP3-expressing neurons in an acute cerebral cortical slice imaged by RAMP with the low magnification light path. Several neurons are seen in L2/3.

(C) Representative single-trial single-voxel voltage recording of spontaneous activity recorded from the two colored neurons simultaneously in (D). Top, raw (lighter colors) and filtered (50-Hz Butterworth low-pass filter; darker colors) optical traces. Bottom, the traces were corrected for the photobleaching and normalized to the baseline drift (black traces in top).

(D) Top, a two-photon image of ASAP3-expressing neurons with the high-magnification light path. Bottom, magnified views of the boxed regions in top. Colored crosses indicate selected voxels on the plasma membrane for voltage imaging in (C). Scale bar in A, 1 mm; B, 100  $\mu$ m; C, 20  $\mu$ m.

See also [Figure S1](#).

S3C and S4), which is much shorter than that reported with calcium recording in barrel cortex slices ( $SD = 11.7$  ms) ([Ranganathan and Koester, 2010](#)). Lowering the filter cutoff frequency below 50 Hz impacted temporal resolution owing to over-filtering. Higher cutoff frequencies caused insufficient filtering with larger noise, resulting in larger temporal errors in peak detection ([Figure S4](#)). Altogether, we used a Butterworth low-pass filter cutoff at 50 Hz in this study, as it provides not only high SNR but also high time accuracy.

### Capability of AIR

There were no significant differences observed in peak amplitude and SNR between neuron groups that showed regular APs or AP bursts ([Figure S2C](#),  $n = 6$  neurons in each group). During recordings, we

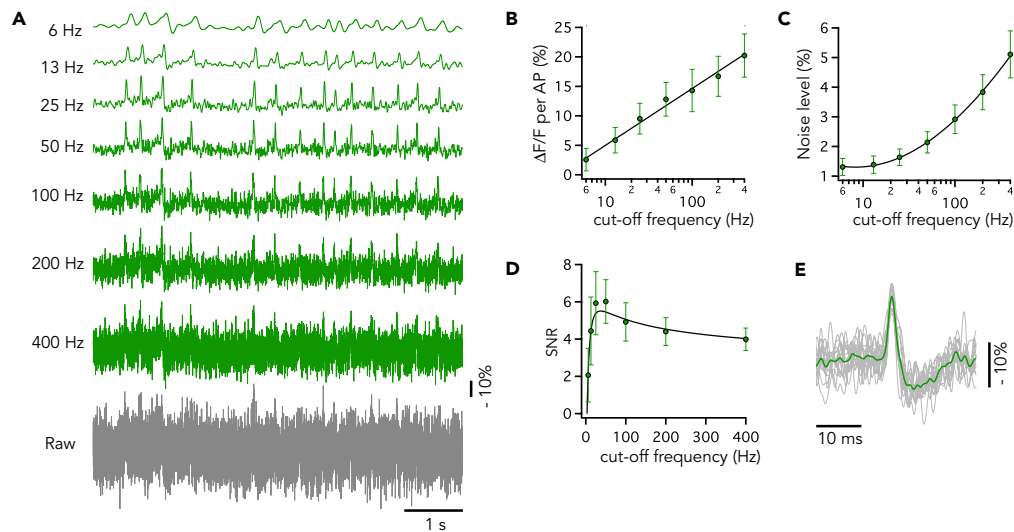


**Figure 2. Effect of Cutoff Frequency of the Noise-Reduction Filter on SNR**

(A) A representative optical regular firing trace (containing 14 fAPs; Raw, not filtered, gray trace) was filtered with Butterworth low-pass filters cutting off at 6–400 Hz (green traces). This record is a part of the dashed box in Figure 4C, and the image of recorded neuron is shown in Figure 4A (green box).

(B) The signal level was linearly correlated with the logarithm of filter frequency ( $\log_{10}(v)$ ).

(C) The noise level was correlated with  $\log_{10}(v)$  by a power law. In (B) and (C), the black lines, symbols, and error bars indicate regressed curve, mean, and SD, respectively.

(D) Relationship between SNR and cutoff frequency. The signal (B) was divided with the noise (C). The black line was calculated by dividing the regression lines in (B) by that in (C). The symbols and error bars indicate mean and SD, respectively.

(E) The 14 fAPs were overlapped, showing uniform kinetics with overshoot and afterhyperpolarization. Gray traces indicate individual fAPs (filtered with a 50-Hz Butterworth low-pass filter), and green plot indicates average of the fAPs. See also Figures S2–S5.

observed bursts, which we defined in this study as fAPs with interval less than 300 ms. Even in high-frequency bursts each fAP was clearly distinguished (Figures S1C and S2A). The shortest interspike interval was 17 ms (Figure S5). In addition, not only the sharp overshoot but also the following afterhyperpolarization was recognized (Figure 2E).

We next evaluated AIR in dendrite. Spontaneous voltage signals were simultaneously recorded from soma and a dendrite of a single cell at a sampling frequency of 10 kHz (Figure 3). fAPs were observed in the dendrite with perfect synchronization to the somatic fAPs with a 0.4-ms delay at the peak and reduced peak amplitudes ( $-\Delta F/F = 14.0 \pm 2.5\%$  at soma and  $9.2 \pm 2.9\%$  at dendrite 33  $\mu\text{m}$  from the soma;  $n = 20$  spikes; Figure 3C). This delay indicates that APs were first generated at or close to the soma and then back propagated to the dendrite. The reduction in the amplitude of fAPs can be attributed to the expected difference in amplitude of APs at soma and in dendrites (Stuart et al., 1997). This result indicates that AIR can report fast subcellular voltage changes of dendritic activity as well as in the soma in single trials to study intracellular membrane potential propagation.

Then, we evaluated AIR's ability to monitor spontaneous activities from multiple neurons simultaneously. It requires sufficient SNR for single-trial and single-voxel recording at high sampling rate. In the example presented above, optical spikes were easily identified in the fluorescence intensity time course traces recorded at 10 kHz from 2 voxels, where dwell time for each voxel was 38.5  $\mu\text{s}$ . Since dwell time is important for good SNR, to record more neurons simultaneously with sufficient SNR we reduced the sampling rate to 2 kHz to keep dwell time above tens of microseconds. At 2 kHz, spontaneous optical spikes could be clearly detected from multiple neurons with adequate SNR. For example, in Figure 4, the three neurons showed synchronized bursts and unsynchronized regular fAPs, with SNR >5. When the number of recorded neurons was further increased to 6, dwell time was about 72  $\mu\text{s}$  and the SNR was still adequate (>5) for detecting spontaneous fAPs (Figure S6). These results indicate that AIR can monitor spontaneous firing from multiple neurons in tissue.

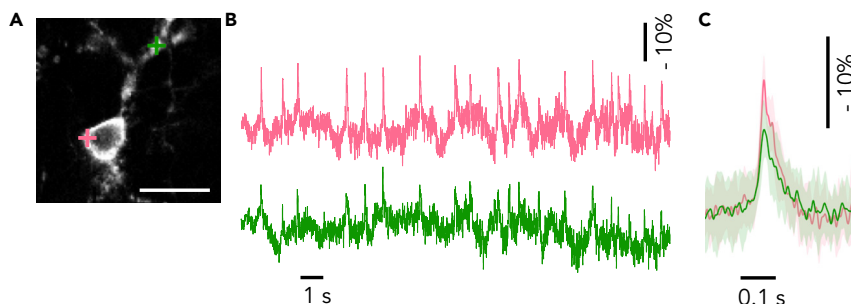


**Figure 3. Membrane Potentials Recorded in Dendrite and Soma**

(A) Representative simultaneous recording of spontaneous somatic (pink) and dendritic (green) activities in a neuron. The recording was performed under RAMP with the high magnification light path. Scale bar: 20  $\mu$ m.

(B) Spontaneous activities in the color-matched recording points in (A), recorded at 10 kHz. SNRs in pink and green were 4.3 and 4.0, respectively.

(C) Averaged spike traces taken in the two locations in (B). Traces were aligned to onset of somatic activity. The shaded regions denote SD.

Target cortical layers for transfection can be selected by simply adjusting the timing of IUE. IUE at embryonic day (E) 13.5 led to ASAP3 expression in L5 neurons (Figure S7). IUE done at E14.5 enabled voltage recording in L4 and L2/3 neurons (Figure S8), which permitted monitoring both intra- and inter-laminar neuronal activities. With different electroporation parameters, neuronal activities in other brain areas can be monitored. Figure S9 shows an example recorded in hippocampus. Altogether, AIR can be used to record intra-laminar/inter-laminar activities in cortex and neuronal activity in other brain regions.

Next, we explored whether AIR could report voltage changes over long time courses. Because SNR is related to the square root of emission photon flux, SNR tended to decrease during long recordings owing to photobleaching. In this study we observed an  $\sim 40\%$  decrease in fluorescence during the first 3 min owing to the small recording volume. Because photobleaching is limited to the vicinity of the recording spot, the recording voxel was moved to different locations on the same cell body every 1–3 min to reduce the photobleaching and maintain adequate SNR. This suspended optical recordings for several seconds when the laser spot was moved to a new location. Figures 5 and S10 show an example of a long-duration recording: membrane potential changes of two neurons were tracked for 14 min in total, and fAPs were easily identified throughout the recording. During the recording, the peak amplitude of fAPs tended to reduce by  $7.8 \pm 3.5\%$  (Figure 5D;  $p > 0.05$ , paired t test,  $n = 7$  neurons), whereas SNR reduced by  $9.5 \pm 2.7\%$  ( $p < 0.05$ , paired t test), but both were still sufficient for reliable peak detection ( $\text{SNR}_{14\text{min}} = 5.4 \pm 0.6$ ). No obvious difference is observable between the fAP waveforms at the beginning and the end of the 14 min recording (Figure S10C), indicating that the long-duration exposure did not affect the cell healthiness. In some cases, we were able to monitor neuronal activity for  $>20$  min with fAPs clearly distinguishable throughout (Figure S11).

### Functional Connectivity Revealed by Jitter-Based Analysis

By virtue of the long-duration recording capability of AIR, we monitored neuronal activities in somatosensory cortex L2/3 and investigated functional connectivity between neurons, which is defined as the correlation of the activities of pairs of neurons (Park and Friston, 2013), by a correlation analysis, Jitter-based method (Agmon, 2012). Jitter-based analysis provides a robust and well-normalized correlation index, Jitter-based synchrony index (JBSI), which allows valid comparison of correlation strength among neuron pairs from different experiments. In an example (Figure 6), neurons 1, 2, and 3 were correlated with each other. And the 1-2 pair had stronger correlation than the 2-3 and 1-3 pairs (JBSI = 0.550, 0.326, and 0.308, respectively), whereas neurons 4 and 5 fired a lot of spikes (99 and 175 spikes, respectively) but had no significant correlation with other neurons.

Of 106 pairs of L2/3 neurons from 13 mice that had more than 6 fAPs, 46 pairs were judged to be statistically correlated ( $p < 0.05$ ), with considerable variability in correlation strength (Figure 7A). Within the significantly correlated neuron pairs, neuron pairs with shorter horizontal distance tended to be more highly correlated (Figure 7B), which is consistent with previous studies using electrophysiology (Holmgren

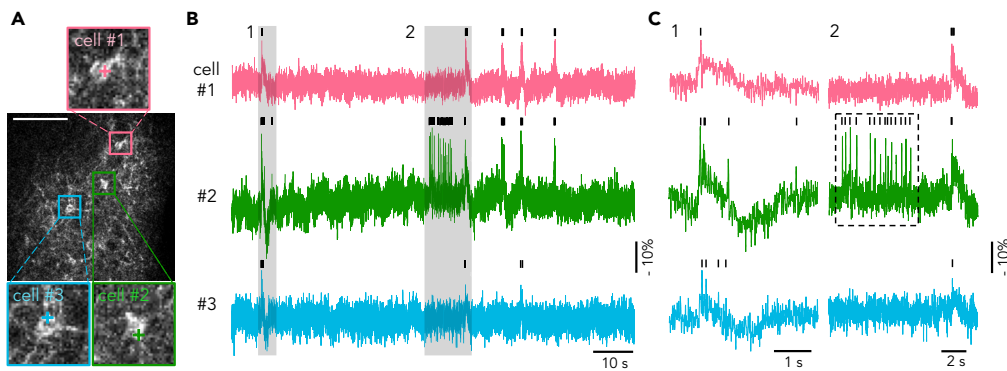


**Figure 4. Simultaneous Voltage Recording from Multiple Cells**

(A) Image of recorded neurons. The recording was performed under the low-magnification light path. Regions in colored boxes are magnified to show recorded cells. Colored crosses indicate recording points. Scale bar: 100  $\mu$ m.

(B) Spontaneous activities in the color-matched neurons in (A), recorded at 2 kHz. SNRs of cells #1–3 were 4.6, 5.0, and 4.1, respectively.

(C) Shaded areas in (B) are expanded, showing clearly distinguishable fAPs in bursts (C1) and regular firing (C2, dashed box). Small vertical bars on the top of traces indicate spike events detected.

See also [Figures S6–S9](#).

[et al., 2003](#)), photo-stimulation ([Boucsein et al., 2011](#)) or calcium imaging ([Cheng et al., 2011](#)). Neuron pairs with shorter horizontal distance had shorter delay of correlation than pairs with longer distance ([Figure 7C](#)).

In somatosensory cortex, neurons in L2/3 have intralaminar horizontal connections ([Thomson, 2007](#)). However, the postnatal developmental time course of the functional connections has not yet been fully understood at cellular resolution. To investigate the development of functional connections in L2/3 of somatosensory cortex, we recorded spontaneous activities of multiple neurons simultaneously in acute slices from postnatal day (P) 7 to P17 mice and analyzed activity correlations between neuron pairs. In [Figure 8A](#), data were taken from all active neurons found in fields of view irrespective of how they correlated with each other. In slices from the youngest stage (P7–9), L2/3 neurons were rarely correlated ([Figure 8A](#), left; median JBSI = 0.08 [0, 0.21],  $n = 27$  neuron pairs from 4 animals). The correlation strength of neuron pairs increased at the P10–12 state (0.21 [0.15, 0.32],  $n = 29$  from 3 animals) and further at the P13–15 stage (0.34 [0.26, 0.50],  $n = 19$  from 3 animals). And, in P13 and older slices, the correlation strength remained high. Distribution of the horizontal distance of all imaged neuron pairs did not differ much along the developmental stages ([Figure 8A](#), right). Therefore, the age-dependent increase in the correlation strength does not reflect a bias in distances between imaged neurons. These results thus suggest that somatosensory cortex L2/3 neurons increase in horizontal functional connection strength during the second postnatal week. This is consistent with previous electrophysiological studies ([Stern et al., 2001](#); [Wen and Barth, 2011](#)), with the AIR approach providing higher throughput with better spatial resolution.

We next asked whether the timing of L2/3 functional connectivity can be inferred from the time course of development. When neuron pairs with significant correlation were extracted, the correlation strength was within a similar range and did not show a developmental change ([Figure 8B](#), left). However, the horizontal distance of the correlated pairs was very short at P7–9 ([Figure 8B](#), right), indicating that the L2/3 neurons are connected only with adjacent neurons at this stage. In the later stages (P10–12 and P13–15), correlated L2/3 neurons were located further apart. Thus, the developmental increase in correlation strength when all neuron pairs were tested irrespective of correlation ([Figure 8A](#), left) is mainly attributed to increased correlation between distant neurons in late stages rather than increased correlation in each correlated neuron pair. This result is consistent with previous electrophysiological studies ([Wen and Barth, 2011](#)), but with better spatial resolution.

Moreover, in the early stage ( $P < 13$ ), the strength of functional connectivity was not significantly related with the horizontal distance of neurons. Whereas in the later stage ( $P \geq 13$ ), the function connectivity was significantly negatively correlated with the distance (Pearson's correlation test:  $P = 0.016$ ,  $r = -0.42$ ; Spearman's rank correlation test:  $P = 0.004$ ,  $r = -0.49$ ; [Figure 8C](#)). These results indicate that the

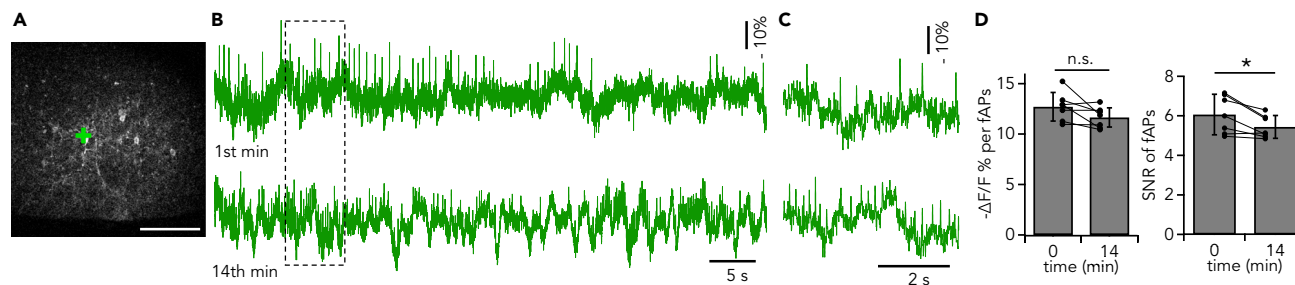


**Figure 5. A Long-Duration Recording**

(A) Image of field of view. Crosses indicate recording points. Scale bar: 100 μm.

(B) Optical traces of AIR imaging show the first (top) and last minute (bottom) of a total 14 min recording. SNR of the entire recording period was 5.0.

(C) Framed areas in (B) are expanded. Optical spikes are clearly distinguished throughout the recording.

(D) Pair-matched comparison of peak amplitude (left) and SNR (right) between the optical traces of the first and last minutes. Mean ± SD together with values from each cell are shown. \* $p < 0.05$ , paired t test.

See also [Figures S10](#) and [S11](#).

distance-dependent functional connections emerged after P13, consistent with previous electrophysiological studies ([Erzurumlu and Gaspar, 2012](#); [Wen and Barth, 2011](#)) but with better spatial resolution.

## DISCUSSION

Through the continuing development of voltage indicators and the advances in microscopy, fast voltage imaging is increasingly coming to the forefront of neuroscience as a powerful tool complementary to calcium imaging and electrophysiology for dissecting neuronal circuits. Although widely anticipated, voltage imaging is less widespread than calcium imaging owing to intrinsic constraints related to indicator targeting to the membrane and the fast nature of electrical signals. To overcome these limitations, we utilized a recently developed high-performance GEVI, ASAP3, and achieved strong and sparse indicator expression in the mouse brain via IUE. To record ASAP3 signals, we used RAMP, which enables multiple cell recording with high sampling rates (2–10 kHz) by scanning only selected points. The combination of ASAP3, IUE, and RAMP enabled simultaneous monitoring of electrical activity from multiple neurons in brain tissue over the course of tens of minutes. This permitted analysis of functional connectivity in circuit with better throughput and greater accuracy than previously possible.

### Subthreshold Events

Calcium imaging cannot report hyperpolarizing (inhibitory) and subthreshold depolarizing (excitatory) signals that occur continuously in most neurons ([Knöpfel and Song, 2019](#)). One advantage of voltage imaging is the potential to readout subthreshold neuronal activity. In AIR recording, not only the sharp overshoots but also following afterhyperpolarizations were recognized from fAPs ([Figure 2E](#)). The baseline fluctuations of fluorescence intensity may possibly reflect subthreshold membrane potential changes (e.g., [Figures 4](#), [S1](#), [S2A](#), and [S6B](#)). However, there is a difficulty in segregation of these slow signal changes from tissue motion artifacts, especially in slow second-order changes. ULoVE that uses holographically generated array of excitation foci may be robust against the tissue motion artifacts, which is capable of steady recording even in *in vivo* brain ([Villette et al., 2019](#)). The apparent baseline fluctuations and shagginess seen in some figures (e.g., [Figures 6](#) and [S8](#)), aside from whether they reflect the real membrane potential changes or motion artifacts, did not affect the spike detection: calculated SNR of such traces did not differ from less noisy looking traces (e.g., [Figures 2](#) and [S7](#)). SNR ranged 4.2–6.0 in the former and 4.1–7.2 in the latter. The noise level was calculated after removing the slow baseline fluctuations by baseline correction (see [Transparent Methods](#)); thus, we consider that the apparent shagginess in some traces were not relevant to the noise level for spike detection.

### Comparison between IUE and Viral Delivery

In this study, we used IUE to express the voltage indicator in somatosensory cortex and investigated functional connection in the upper layers. As the target selection of IUE is very flexible, neurons in other cortical layers and brain regions, e.g., hippocampus, can be labeled with IUE ([Matsui et al., 2011](#); [Navarro-Quiroga et al., 2007](#); [Szczyrkowska et al., 2016](#)). And specific types of cells can be targeted by the promoter choice.

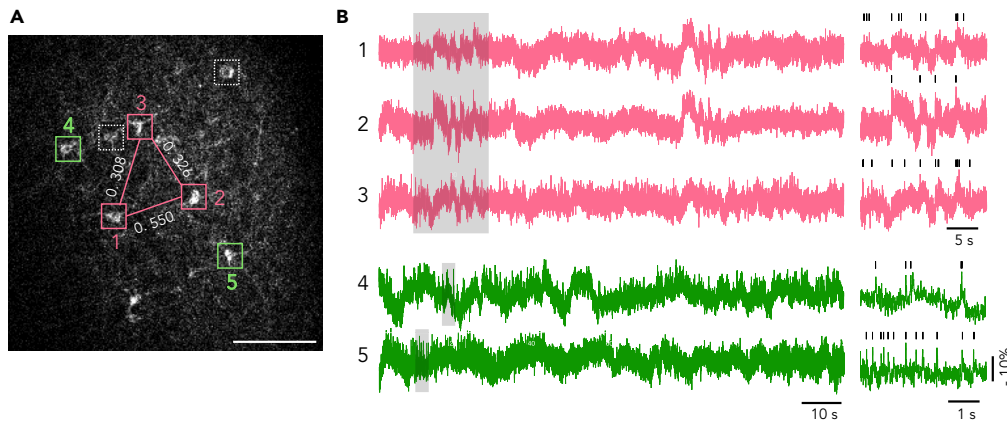


**Figure 6. Pairwise Correlations of Neurons by Spike Timing**

(A) ASAP3 expressing in L2/3 neurons in a slice (P13). Five neurons showed more than six fAPs (colored boxes) (SNR of cells 1–5 were 4.3, 5.1, 4.7, 5.0, and 4.9, respectively), and the other two (white dashed boxes) were silent. Pairwise correlations between each neuron pair was calculated. The three neurons in pink boxes were significantly correlated. Strength of pairwise correlation is indicated by white figures. The two neurons in green boxes were firing but not significantly correlated with neurons in pink boxes or with each other. The white numbers above pink lines show JBSI values of pairs. Scale bar: 100  $\mu\text{m}$ .

(B) Spontaneous activities in the neurons displayed in (A). The three pink traces exhibited several synchronized fAPs as well as unsynchronized fAPs, whereas the two green traces only had unsynchronized fAPs. Right, shaded areas are expanded, showing synchronized (pink) and unsynchronized (green) neurons. Detected fAPs are marked by vertical bars.

IUE provides relatively sparse but strong expression of GEVI, which is beneficial to multi-cell recording. The optical traces had sufficient quality in SNR (Figures S12A and S12B). There was a positive correlation between the signal intensity and SNR, but there was no correlation between the detected spike number and SNR (Figures S12C and S12D). Sparse and strong expression pattern has also been achieved via viral delivery with a soma-targeting tag sequence. For example, adding a Kv2.1 proximal retention and clustering sequence to GEVIs results in enrichment of the indicator protein at soma (Abdelfattah et al., 2019; Adam et al., 2019; Villette et al., 2019). However, it hinders monitoring voltage from dendrites and axons (Quicke et al., 2019). Without a soma-targeting tag sequence, fluorescence signals from dendrites and axons would be hidden by overlapping signals from other neurons with viral expression methods. But the sparse expression pattern by IUE permits isolation of signals from dendrites and axons. Thus, IUE is a good choice for GEVI expression as it allows not only multiple cell recording but also recording in axons and dendrites.

### Comparison between the Jitter-Based Method and the Cross-Correlogram Method

In functional connectivity studies, correlation analysis has been widely used in determining neuron activity synchronicity. Among the correlation analysis methods, cross-correlogram (CCG) (Eggermont, 2010; Ostojic et al., 2009) is a popular graphical method to depict the correlation features of neuron pairs. And Excess Coincidence Index (ECI) (Alonso et al., 2008) and Cross-Correlation Coefficient (CCC) (Roy and Alloway, 2001) are the most employed CCG-based correlation indices. Because CCG and these indices are based on the assumption that spike trains are stationary Poisson processes, they have serious limitations when used in real spike trains. When the firing rate is not stable throughout but have local alterations or spike bursts are inserted intermittently, CCG analysis results in erroneous evaluation of synchrony, and its improperly normalized correlation indices are not suitable for comparisons of correlation strength between cell pairs.

In this study, we adopted the Jitter-based method to avoid these issues: it does not rely on such assumptions of stationary firing rate and Poisson distribution of spike timing. CCGs constructed from neuron pairs that were judged as correlated by the Jitter-based method show clear peaks close to the zero lag, and those from neuron pairs judged as uncorrelated do not (Figures S13B–S13D). Some neuron pairs were judged as correlated by the Jitter-based method with relatively long delay (15–22 ms; Figures 7C and S13C). The digital filter cutting off at 50 Hz impacted the accuracy of the AP timing, which makes the

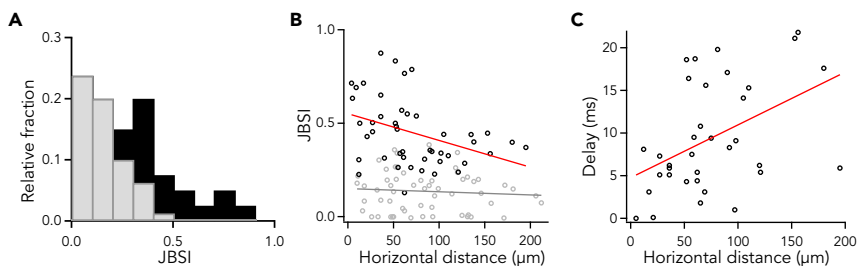


**Figure 7. Pairwise Correlations of Firing Neurons**

(A) Histogram showing the fractional occurrence of JBSI of 106 neuron pairs from all mice (P7–P17). Black bars indicate synchronized pairs ( $Z$  score  $>1.96$ ), and gray bars indicate not synchronized ones.

(B) JBSI was negatively correlated with horizontal distance in significantly correlated neuron pairs (black dots; Pearson’s correlation coefficient =  $-0.37$ ,  $p = 0.01$ ; Spearman’s rank correlation:  $r = -0.39$ ,  $p = 0.007$ ) but not in uncorrelated pairs (gray dots; Pearson’s correlation coefficient =  $-0.08$ ,  $p = 0.55$ ; Spearman’s rank correlation:  $r = -0.05$ ,  $p = 0.68$ ). Red and gray lines indicate linear regression of the synchronous and asynchronous pairs, respectively.

(C) A positive correlation between the delay of correlation and horizontal distance in significantly correlated neuron pairs (35 neuron pairs from 9 mice; Pearson’s correlation coefficient =  $0.44$ ,  $p = 0.007$ ; Spearman’s rank correlation:  $r = 0.44$ ,  $P = 0.009$ ).

See also [Figures S12](#) and [S13](#).

CCG distribution wider but should not alter the center of the CCG distribution if the number of spike event is large enough: the full width at half maximum of the central peak of the CCG calculated from two points of the same cell body was 8 ms, not satisfactorily short, but the center was very close to the zero lag ([Figure S13A](#)). Thus the relatively long delays in some neuron pairs may be due to small spike pair number or reflect actual long delay of neuron correlations. It is beneficial that Jitter-based analysis can judge correlation of neuron pairs with relatively small number of spikes, but issues arising from the small spike number should be paid attention.

The Jitter-based method provides a well-normalized index, JBSI, that allows valid comparisons of correlation strength of neuron pairs recorded in different experiments or even by different investigators ([Agmon, 2012](#)). Using JBSI, we were able to detect correlation of neuron pairs with not stationary firing rates and burst spiking and to compare strength of correlation among neurons recorded in different experimental conditions.

Although we only focused on excitatory correlations such as synaptic connections and common inputs in this study, further analyses on inhibitory correlation and non-spiking activity with different analysis methods would provide more information about neuronal circuits.

### Functional Connectivity between L2/3 Neurons in Somatosensory Cortex

Neurons in somatosensory cortex L2/3 have intralaminar connection ([Thomson, 2007](#)). Previous studies employing electrophysiology ([Holmgren et al., 2003](#)), photostimulation ([Boucsein et al., 2011](#)), or calcium imaging ([Cheng et al., 2011](#)) demonstrated a negative association between horizontal distances of neurons and their correlation strength after postnatal development. Using ASAP3, we observed a similar negative association ([Figure 7B](#)), and the distance-dependent functional connections were only observed after P13 ([Figure 8C](#)).

As the maturation of the cortical circuit is important for the postnatal brain development, we further investigated how the pairwise correlations of L2/3 neurons in somatosensory cortex change during development. Previous studies have reported that P13–16 is critical for horizontal connections in L2/3 ([Wen and Barth, 2011](#)) with electrophysiological methods such as field stimulation and/or field recording. In this study, we observed an increase in overall correlation strength between the P7–9 and P13–15 periods ([Figure 8A](#), left). And we found that neurons were synchronized only with adjacent neurons in early stages, whereas they formed significant functional connections with distant neurons in later stages. This result raises additional evidence for a critical period in L2/3 functional connections.

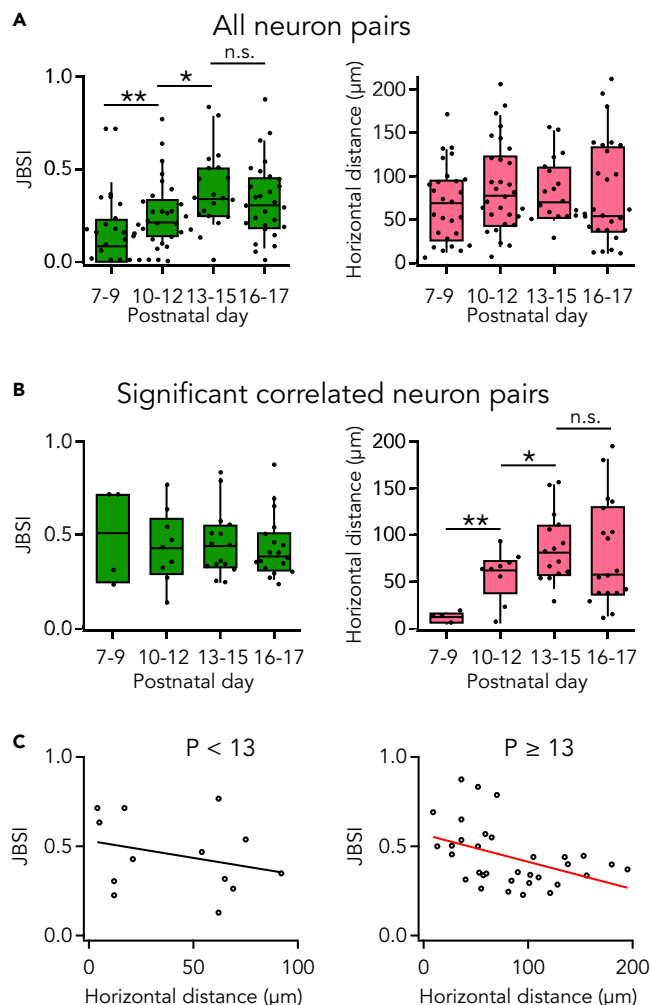


**Figure 8. Developmental Changes in Neuronal Correlation in Layer 2/3**

(A) Strength of synchrony (left) and horizontal distance (right) at different postnatal stages in all neuron pairs ( $n = 27, 29, 19,$  and  $28$  pairs for stages P7–9, P10–12, P13–15, and P16–17, respectively). Left, synchrony index in JBSI increased along the developmental stages. Right, there was no obvious difference in horizontal distance of neuron pairs among different stages. (B) Synchrony strength (left) and horizontal distance (right) of significantly correlated pairs at different postnatal stages ( $n = 4, 9, 15,$  and  $18,$  respectively). Left, synchrony index was similar among the stages. Right, the horizontal distance of neuron pairs at P7–9 was much shorter than at other stages, and that at P10–12 was also shorter than at P13–15. In (A) and (B), box plots show IQR, range (10–90%), and median, \*:  $p < 0.1$ ; \*\*:  $p < 0.01$ , Mann-Whitney U-test.

(C) Correlation between JBSI and horizontal distance in significantly correlated neuron pairs from younger and older mice. In the younger mice ( $P < 13$ , left), the correlation was not significant (Pearson’s correlation test:  $P = 0.34$ ; Spearman’s rank correlation test:  $P = 0.50$ ), whereas in older mice ( $P \geq 13$ , right), the strength of synchrony was significantly negatively associated with horizontal distance between neurons (Pearson’s correlation test:  $r = -0.42$ ,  $P = 0.016$ ; Spearman’s rank correlation test:  $r = -0.49$ ,  $P = 0.004$ ). Black circles indicate significantly correlated pairs, and the black/red line indicates the linear regression line.

See also [Figures S12](#) and [S14](#).

### Comparison with a Study of Pairwise Correlation Using Calcium Imaging and NCC Analysis

A previous study using calcium imaging reported an inconsistent finding that the distance-dependent functional connection in L2/3 disappeared and the network activity was desynchronized at the end of the second postnatal week (Golshani et al., 2009). This seemingly different result, however, may be due to differences in experimental systems. Golshani et al. recorded neuronal activity *in vivo* with an intact thalamo-cortical (TC) circuit, which is crucial for synchronized activity in barrel cortex L4 neurons in neonatal mice (Mizuno et al., 2018): the synchronicity of L4 neurons *in vivo* during first postnatal week highly depends

on TC circuit input, and the refinement of the TC circuits in the second postnatal week leads to desynchronization of L4. Thus, the TC circuits may also affect the synchronicity of L2/3 neurons during development. In coronal cortical slices, these effects by long projection would be eliminated. Because we desired to address only the question of connectivity within cortex, we used coronal cortical slices in which cortex and subcortical structures are disconnected (Agmon and Connors, 1991).

Alternatively, it might be possible that the high temporal detection of our method resulted in more efficient spike detection, thereby leading to different interpretation in spike frequency from the calcium imaging study. Specifically, the earlier study reported that calcium imaging accurately detected bursts but missed 60% of single spikes (Golshani et al., 2009), which is consistent with another study that reported that two-photon calcium imaging failed to detect at least 75% of active cells in somatosensory cortex (Tada et al., 2014). To determine if our results with ASAP3 were consistent with the calcium imaging-based findings, we emulated spike detection by calcium imaging using our spike data with ASAP3 by removing different fractions of single spikes and performing normalized correlation coefficient (NCC) analysis as performed in the previous work (Golshani et al., 2009). When 100% or 60% of single APs were removed, pairwise correlations of neuron pairs were higher in early stages than in late stages (Figure S14 left two panels), opposite to our result using Jitter-based synchrony analysis of all spikes (Figures 8A left and S14B left) and matching the findings of Golshani et al. However, when 30% or none of the single APs were removed, correlations of neuron pairs were not apparently different among the stages (Figure S14A, right two panels). Thus, the fidelity of single AP detection impacts the results of pairwise correlation analysis.

Our analysis also revealed that a developmental increase in neuron connectivity is only apparent in single APs, because it was diminished by removal of all single APs in Jitter-based analysis (Figure S14B, middle) while it was preserved by removal of all APs in bursts (Figure S14B, right). As single spikes became dominant in the late developmental stages than early stages (Figure S14C), failure of the calcium indicator to detect single APs would result in underestimation of the strength of pairwise connection in late stages. A similar effect may explain the weak relationship between horizontal distance and calcium imaging-based correlation at P13 and later (Golshani et al., 2009), compared with our detection of distance-dependent correlation at these stages (Figure 8C right).

Furthermore, correlation analysis methods also affect the evaluation. The NCC analysis is sensitive to the difference in firing rates between neuron pairs and also to the change in the firing rate (Agmon, 2012; Tchumatchenko et al., 2011). In strongly bursting neuron pairs, the NCC analysis tends to overestimate synchrony strength. As neurons in early developmental stage tend to fire in bursts (Figure S14C), the overestimation of NCC would be more overt in early developmental stage than older stages. Our ASAP3 recording resolved not only APs in bursts but also single APs with high fidelity, and the Jitter-based synchrony analysis is not affected by the firing rate difference between neurons and alterations in firing rate. Thus, the ability to detect single APs and obtain their precise timings provides additional sensitivity for functional connectivity analysis.

In summary, we have demonstrated that the combination of ASAP3, IUE, and RAMP was able to report voltage transients from multiple neurons in brain tissue at the single-trial and single-voxel level in long-term recording with a millisecond-scale temporal resolution. In addition, we have shown that the AIR approach enables tracking spontaneous voltage dynamics from multiple subcellular regions such as soma and dendrites simultaneously. AIR approach is more efficient in obtaining large number of cells than multi-patch experiments, less invasive than electrophysiological experiments, and provides better time resolution than calcium imaging. Together with the robust Jitter-based analysis, AIR approach is expected to provide a means to investigate functional network in brain tissue.

### Limitations of the Study

Although two-photon microscopes have been getting popular in neuroscience laboratories, conventional mirror-driven laser scanning types are not suitable for 2D or 3D action potential detection. RAMP is powerful in that point; however, the commercially available RAMP system is expensive and in-house build requires knowledge and experience in optics and computer software development. This difficulty in setting up a RAMP system may hinder wide use of the technique. As discussed above, RAMP with single voxel scanning is susceptible to tissue motion. It would be more evident in *in vivo* recording. The ULoVE illumination is a solution to this issue by splitting laser focus to several spots in the 3D space and enables stable *in vivo* voltage recording (Villette et al., 2019). However, the division of the laser beam reduces laser power at each target voxel, resulting in reduction in the signal intensity. In this study, simple voxel RAMP scanning yielded enough signal intensity, which has a

direct relation to SNR, from multiple cells. To gain similar number of cells recorded at the same time with ULoVE, more laser power or better sensitivity of the voltage sensor would be necessary.

### Resource Availability

#### Lead Contact

Further information and requests for resources and reagents should be directed to and will be fulfilled by the Lead Contact, Takafumi Inoue ([inoue.t@waseda.jp](mailto:inoue.t@waseda.jp)).

#### Materials Availability

This study did not generate new unique reagents.

#### Data and Code Availability

The data that support the findings of this study are available from the corresponding author upon reasonable request.

The custom Python scripts are available from the corresponding author upon request. The custom software, TI Workbench, is available on the web site (<http://inouelab.biomed.sci.waseda.ac.jp/inouelab-web/tiwb.html>).

## METHODS

All methods can be found in the accompanying [Transparent Methods supplemental file](#).

## SUPPLEMENTAL INFORMATION

Supplemental Information can be found online at <https://doi.org/10.1016/j.isci.2020.101363>.

## ACKNOWLEDGMENTS

This work was supported by Grant-in-Aid for Scientific Research from the Japan Society for the Promotion of Science (JSPS; JP16H06482, K.N.; 23300121, T.I.), Private University Research Branding Project (MEXT, Japan, T.I.), and Waseda University Grants for Special Research Projects (Waseda University, Japan, T.I.).

## AUTHOR CONTRIBUTIONS

All the authors had full access to all the data in this study and take responsibility for the integrity of the data and the accuracy of the data analysis. T.I. and B.L. conceived and designed the research; B.L. performed the research and analyzed the data; Y.K. contributed in molecular biology and microscopy; B.L. learned the IUE protocol from S.Y. and K.N. at K.N.'s laboratory in Keio University School of Medicine; M.C. and M.Z.L. created and provided ASAP3; B.L. and T.I. drafted the manuscript; M.C. and M.Z.L. provided critical revision of the manuscript; T.I. obtained funding.

## DECLARATION OF INTERESTS

The authors declare no competing interests.

Received: February 13, 2020

Revised: April 7, 2020

Accepted: July 9, 2020

Published: August 21, 2020

## REFERENCES

- Abdelfattah, A.S., Kawashima, T., Singh, A., Novak, O., Liu, H., Shuai, Y., Huang, Y.-C., Campagnola, L., Seeman, S.C., Yu, J., et al. (2019). Bright and photostable chemigenetic indicators for extended in vivo voltage imaging. *Science* 365, 699–704.
- Adam, Y., Kim, J.J., Lou, S., Zhao, Y., Xie, M.E., Brinks, D., Wu, H., Mostajo-Radji, M.A., Kheifets, S., Parot, V., et al. (2019). Voltage imaging and optogenetics reveal behaviour-dependent changes in hippocampal dynamics. *Nature* 569, 413–417.
- Agmon, A. (2012). A novel, jitter-based method for detecting and measuring spike synchrony and quantifying temporal firing precision. *Neural Syst. Circuits* 2, 5.
- Agmon, A., and Connors, B.W. (1991). Thalamocortical responses of mouse somatosensory (barrel) cortex in vitro. *Neuroscience* 41, 365–379.
- Alonso, J.-M., Yeh, C.-I., and Stoelzel, C.R. (2008). Visual stimuli modulate precise synchronous firing within the thalamus. *Thalamus Relat. Syst.* 4, 21–34.

- Bayguinov, P.O., Ma, Y., Gao, Y., Zhao, X., and Jackson, M.B. (2017). Imaging voltage in genetically defined neuronal subpopulations with a cre recombinase-targeted hybrid voltage sensor. *J. Neurosci.* *37*, 9305–9319.
- Boucsein, C., Nawort, M., Schnepel, P., and Aertsen, A. (2011). Beyond the cortical column: abundance and physiology of horizontal connections imply a strong role for inputs from the surround. *Front. Neurosci.* *5*, 32.
- Cheng, A., Gonçalves, J.T., Golshani, P., Arisaka, K., and Portera-Cailliau, C. (2011). Simultaneous two-photon calcium imaging at different depths with spatiotemporal multiplexing. *Nat. Methods* *8*, 139–142.
- deCharms, R.C., and Zador, A. (2000). Neural representation and the cortical code. *Annu. Rev. Neurosci.* *23*, 613–647.
- Diba, K., Amarasingham, A., Mizuseki, K., and Buzsáki, G. (2014). Millisecond timescale synchrony among hippocampal neurons. *J. Neurosci.* *34*, 14984–14994.
- Eggermont, J.J. (2010). Pair-correlation in the time and frequency domain. *Analysis of Parallel Spike Trains* (Springer), pp. 77–102.
- Erzurumlu, R.S., and Gaspar, P. (2012). Development and critical period plasticity of the barrel cortex: Barrel cortex plasticity. *Eur. J. Neurosci.* *35*, 1540–1553.
- Fink, A.E., Bender, K.J., Trussell, L.O., Otis, T.S., and DiGregorio, D.A. (2012). Two-photon compatibility and single-voxel, single-trial detection of subthreshold neuronal activity by a two-component optical voltage sensor. *PLoS One* *7*, e41434.
- Golshani, P., Gonçalves, J.T., Khoshkoo, S., Mostany, R., Smirnakis, S., and Portera-Cailliau, C. (2009). Internally mediated developmental desynchronization of neocortical network activity. *J. Neurosci.* *29*, 10890–10899.
- Grienberger, C., and Konnerth, A. (2012). Imaging calcium in neurons. *Neuron* *73*, 862–885.
- Han, K.-S., Guo, C., Chen, C.H., Witter, L., Osorno, T., and Regehr, W.G. (2018). Ephaptic coupling promotes synchronous firing of cerebellar purkinje cells. *Neuron* *100*, 564–578.e3.
- Hebb, D.O. (2005). *The Organization of Behavior: A Neuropsychological Theory* (Psychology Press).
- Holmgren, C., Harkany, T., Svennerfors, B., and Zilberter, Y. (2003). Pyramidal cell communication within local networks in layer 2/3 of rat neocortex. *J. Physiol.* *551*, 139–153.
- Iyer, V., Hoogland, T.M., and Saggau, P. (2006). Fast functional imaging of single neurons using random-access multiphoton (RAMP) microscopy. *J. Neurophysiol.* *95*, 535–545.
- Jadhav, S.P., Wolfe, J., and Feldman, D.E. (2009). Sparse temporal coding of elementary tactile features during active whisker sensation. *Nat. Neurosci.* *12*, 792–800.
- Jouhanneau, J.-S., Kremkow, J., and Poulet, J.F.A. (2018). Single synaptic inputs drive high-precision action potentials in parvalbumin expressing GABA-ergic cortical neurons in vivo. *Nat. Commun.* *9*, 1540.
- Knöpfel, T., and Song, C. (2019). Optical voltage imaging in neurons: moving from technology development to practical tool. *Nat. Rev. Neurosci.* *20*, 719–727.
- Kuhn, B., Denk, W., and Bruno, R.M. (2008). In vivo two-photon voltage-sensitive dye imaging reveals top-down control of cortical layers 1 and 2 during wakefulness. *Proc. Natl. Acad. Sci. U S A* *105*, 7588–7593.
- Kulkarni, R.U., and Miller, E.W. (2017). Voltage imaging: pitfalls and potential. *Biochemistry* *56*, 5171–5177.
- Matsui, A., Yoshida, A.C., Kuboya, M., Ogawa, M., and Shimogori, T. (2011). Mouse in utero electroporation: controlled spatiotemporal gene transfection. *J. Vis. Exp.* *54*, e3024.
- Mizuno, H., Ikezoe, K., Nakazawa, S., Sato, T., Kitamura, K., and Iwasato, T. (2018). Patchwork-type spontaneous activity in neonatal barrel cortex layer 4 transmitted via thalamocortical projections. *Cell Rep.* *22*, 123–135.
- Navarro-Quiroga, I., Chittajallu, R., Gallo, V., and Haydar, T.F. (2007). Long-term, selective gene expression in developing and adult hippocampal pyramidal neurons using focal in utero electroporation. *J. Neurosci.* *27*, 5007–5011.
- Ostojic, S., Brunel, N., and Hakim, V. (2009). How connectivity, background activity, and synaptic properties shape the cross-correlation between spike trains. *J. Neurosci.* *29*, 10234–10253.
- Park, H.-J., and Friston, K. (2013). Structural and functional brain networks: from connections to cognition. *Science* *342*, 1238411.
- Peterka, D.S., Takahashi, H., and Yuste, R. (2011). Imaging voltage in neurons. *Neuron* *69*, 9–21.
- Quicke, P., Song, C., McKimm, E.J., Milosevic, M.M., Howe, C.L., Neil, M., Schultz, S.R., Antic, S.D., Foust, A.J., and Knöpfel, T. (2019). Single-neuron level one-photon voltage imaging with sparsely targeted genetically encoded voltage indicators. *Front. Cell. Neurosci.* *13*, 39.
- Ranganathan, G.N., and Koester, H.J. (2010). Optical recording of neuronal spiking activity from unbiased populations of neurons with high spike detection efficiency and high temporal precision. *J. Neurophysiol.* *104*, 1812–1824.
- Roy, S., and Alloway, K. (2001). Coincidence detection or temporal integration? What the neurons in somatosensory cortex are doing. *J. Neurosci.* *21*, 2462–2473.
- Sadakane, O., Masamizu, Y., Watakabe, A., Terada, S.-I., Ohtsuka, M., Takaji, M., Mizukami, H., Ozawa, K., Kawasaki, H., Matsuzaki, M., et al. (2015). Long-term two-photon calcium imaging of neuronal populations with subcellular resolution in adult non-human primates. *Cell Rep.* *13*, 1989–1999.
- Salomé, R., Kremer, Y., Dieudonné, S., Léger, J.-F., Krichevsky, O., Wyart, C., Chatenay, D., and Bourdieu, L. (2006). Ultrafast random-access scanning in two-photon microscopy using acousto-optic deflectors. *J. Neurosci. Methods* *154*, 161–174.
- Stern, E.A., Jaeger, D., and Wilson, C.J. (1998). Membrane potential synchrony of simultaneously recorded striatal spiny neurons in vivo. *Nature* *394*, 475–478.
- Stern, E.A., Maravall, M., and Svoboda, K. (2001). Rapid development and plasticity of layer 2/3 maps in rat barrel cortex in vivo. *Neuron* *31*, 305–315.
- St-Pierre, F., Marshall, J.D., Yang, Y., Gong, Y., Schnitzer, M.J., and Lin, M.Z. (2014). High-fidelity optical reporting of neuronal electrical activity with an ultrafast fluorescent voltage sensor. *Nat. Neurosci.* *17*, 884–889.
- Stuart, G., Schiller, J., and Sakmann, B. (1997). Action potential initiation and propagation in rat neocortical pyramidal neurons. *J. Physiol.* *505*, 617–632.
- Svoboda, K., and Yasuda, R. (2006). Principles of two-photon excitation microscopy and its applications to neuroscience. *Neuron* *50*, 823–839.
- Szczurkowska, J., Cwetsch, A.W., dal Maschio, M., Ghezzi, D., Ratto, G.M., and Cancedda, L. (2016). Targeted in vivo genetic manipulation of the mouse or rat brain by in utero electroporation with a triple-electrode probe. *Nat. Protoc.* *11*, 399–412.
- Tabata, H., and Nakajima, K. (2008). Labeling embryonic mouse central nervous system cells by in utero electroporation. *Dev. Growth Differ.* *50*, 507–511.
- Tada, M., Takeuchi, A., Hashizume, M., Kitamura, K., and Kano, M. (2014). A highly sensitive fluorescent indicator dye for calcium imaging of neural activity in vitro and in vivo. *Eur. J. Neurosci.* *39*, 1720–1728.
- Tchumatchenko, T., Geisel, T., Volgushev, M., and Wolf, F. (2011). Spike correlations – what can they tell about synchrony? *Front. Neurosci.* *5*, 68.
- Thomson, A.M. (2007). Functional maps of neocortical local circuitry. *Front. Neurosci.* *1*, 19–42.
- Usrey, W.M., and Reid, R.C. (1999). Synchronous activity in the visual system. *Annu. Rev. Physiol.* *61*, 435–456.
- Villette, V., Chavarha, M., Dimov, I.K., Bradley, J., Pradhan, L., Mathieu, B., Evans, S.W., Chamberland, S., Shi, D., Yang, R., et al. (2019). Ultrafast two-photon imaging of a high-gain voltage indicator in awake behaving mice. *Cell* *179*, 1590–1608.e23.
- Wen, J.A., and Barth, A.L. (2011). Input-specific critical periods for experience-dependent plasticity in layer 2/3 pyramidal neurons. *J. Neurosci.* *31*, 4456–4465.
- Xu, H., Furman, M., Mineur, Y.S., Chen, H., King, S.L., Zenisek, D., Zhou, Z.J., Butts, D.A., Tian, N., Picciotto, M.R., et al. (2011). An instructive role for patterned spontaneous retinal activity in mouse visual map development. *Neuron* *70*, 1115–1127.

**iScience, Volume 23**

## **Supplemental Information**

### **Two-Photon Voltage Imaging of Spontaneous Activity from Multiple Neurons Reveals Network Activity in Brain Tissue**

**Binglun Li, Mariya Chavarha, Yuho Kobayashi, Satoshi Yoshinaga, Kazunori Nakajima, Michael Z. Lin, and Takafumi Inoue**

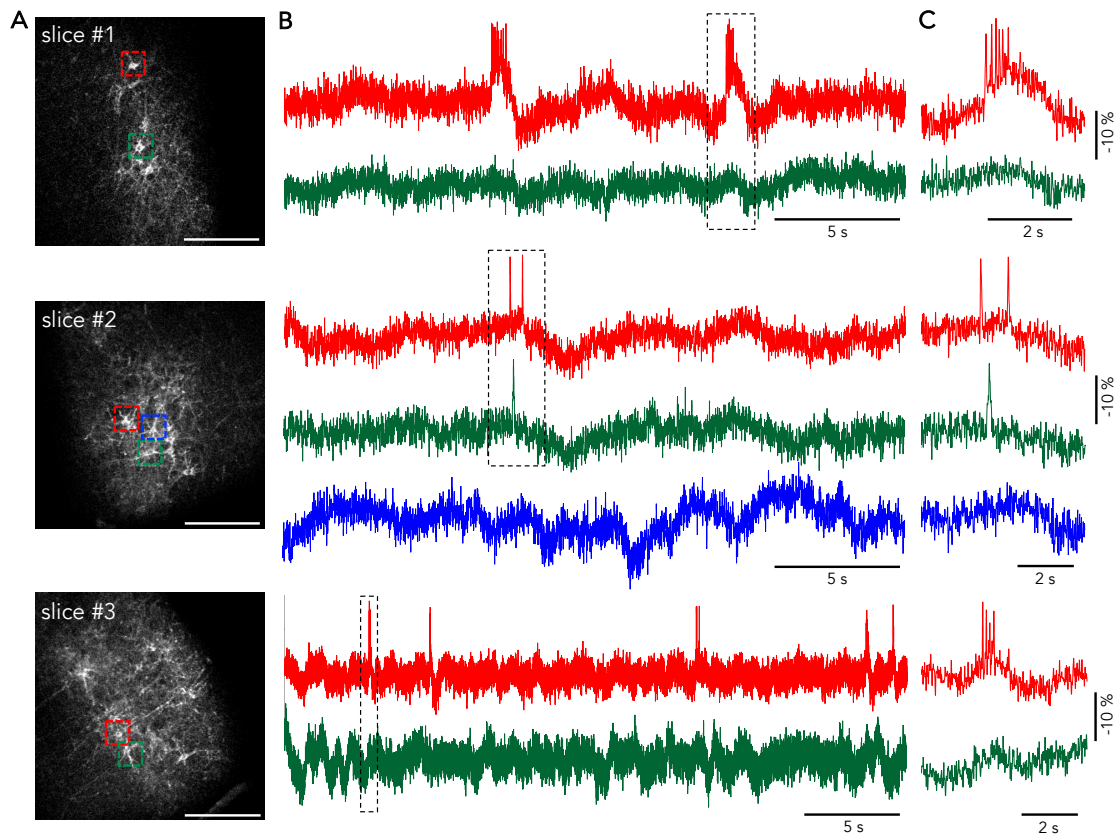


**Figure S1.** Three additional examples of single-trial and single-voxel recording in acute slice in cortical layer 2/3. Related to Figure 1.

**(A)** Cells in the colored boxes were recorded. Scale bar: 100  $\mu\text{m}$ .

**(B)** Spontaneous activities in the color-matched neurons in **A**, recorded at 2 kHz. All 3 examples include both active and silent neurons.

**(C)** Dashed boxes in **B** are expanded, showing clearly distinguishable spikes in bursts (slices #1 and #3) and regular firing (slice #2).

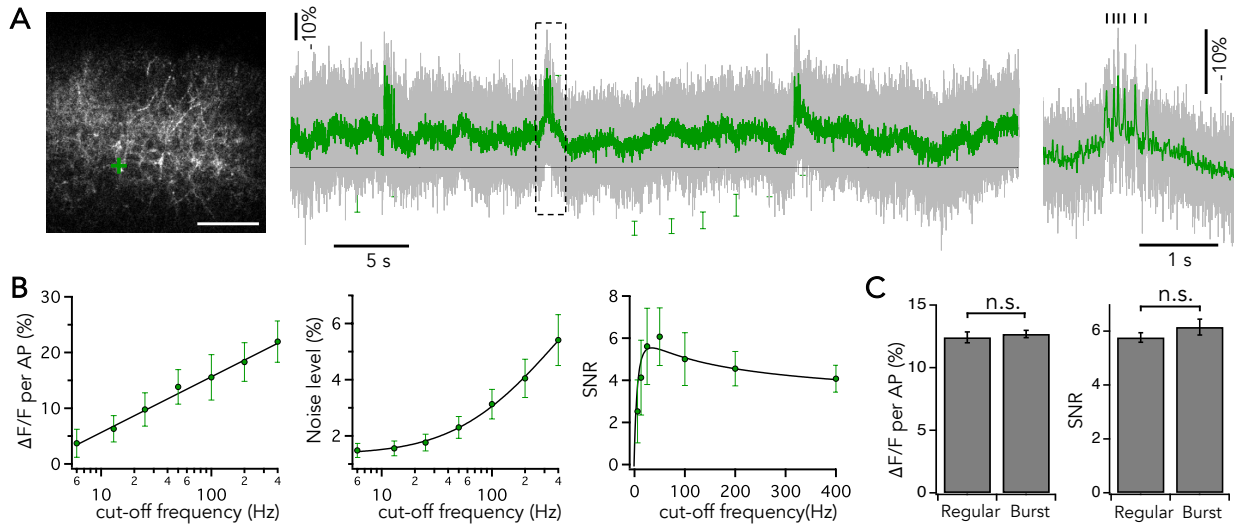


**Figure S2.** Effect of cut-off frequency on SNR in bursty neurons. Related to Figure 2.

- (A)** A representative burst firing in L2/3 neurons in a slice (P9). Left, a bursting neuron (green cross). Scale bar: 100  $\mu\text{m}$ . Middle, a burst firing trace recorded from the marked neuron. Right, expanded view of the dashed box. Fast and narrow spikes are clearly separated. The grey lines show the unfiltered optical traces, and the green lines show filtered traces (cut-off at 50 Hz, SNR = 6.1).
- (B)** The burst spike train shown in the middle panel of **A** was analyzed in the same way as was done in Figure 2. The fitting curve (black) in the right graph has maximum SNR at 41 Hz. The black lines, symbols and error bars indicate regressed curve, mean and SD, respectively.
- (C)** In filtered traces, signal size (left) and SNR (right) of regular fAPs ( $n = 291$  spikes in 6 cells) and fAPs in bursts ( $n = 214$  spikes in 6 cells) has no significant difference (Student's t-test). Means and SDs are shown by bars and error bars.

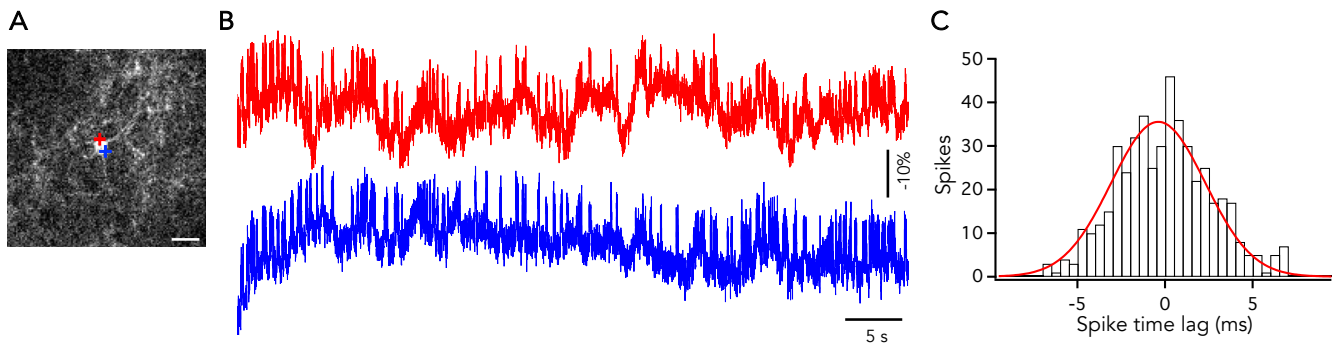


**Figure S3.** Recording two points on the same soma reveals spike timing accuracy. Related to Figure 2.

- (A)** Two-point recording from single soma. Colored crosses indicate the recording locations. Scale bar: 20  $\mu\text{m}$
- (B)** Representative two-point recording recorded at 2 kHz, filtered with 50 Hz low-pass filter. The two traces show synchronized spikes. SNR of the red and blue traces were 4.3 and 4.6, respectively.
- (C)** Distribution of spike time lag ( $T_{a_i} - T_{b_i}$ , refer to Transparent Methods) in two-point recordings from single soma ( $n = 479$  spike pairs in 4 neurons). Red line shows a Gaussian fit of the histogram (center: -0.19 ms; SD: 2.26 ms). In calcium imaging with RAMP, the SD of relative timing error is 11.74 ms.

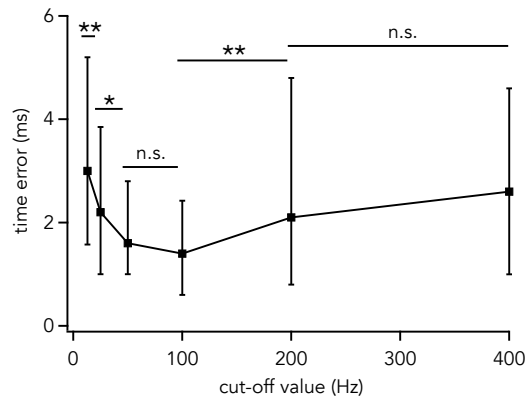


**Figure S4.** Effect of the cut-off frequency on spike timing accuracy. Related to Figure 2.

Errors in peak-time detection were determined as the differences in peak time between pairs of optical spikes recorded at two locations of the same soma simultaneously. At filter cut-off frequency of 50 Hz the time error was 1.6 [1, 2.8], which had no significant difference with time error at 100 Hz. While, at lower and higher cut-off frequencies, the time errors were significantly larger than those of 50 and 100 Hz. Square markers and bars represent median and inter-quartile range. \*:  $p < 0.1$ ; \*\*:  $p < 0.01$ , Mann-Whitney U-test corrected with Holm-Bonferroni method for multiple comparisons ( $n = 4$  neurons, containing 152 spikes for each group).

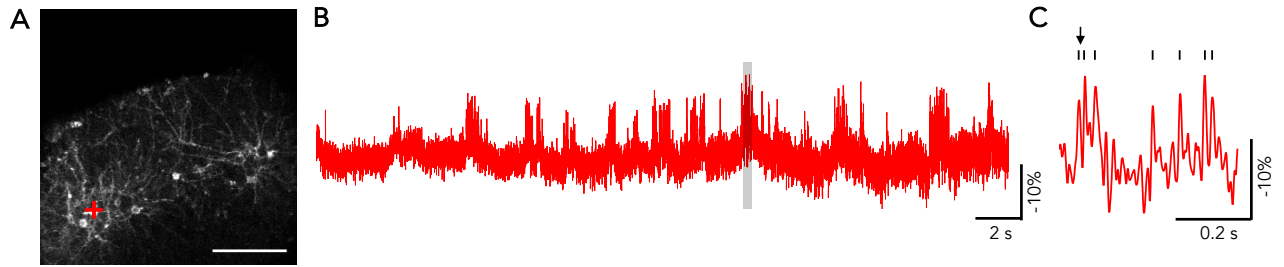


**Figure S5.** Fast AP trains resolved by AIR. Related to Figure 2.

- (A)** An image showing ASAP3 expressing neurons in L 2/3 in somatosensory cortex in brain slice at P16. Scale bar: 100  $\mu\text{m}$ .
- (B)** Optical recording taken from the red cross in **A**. SNR was 4.5.
- (C)** A part of optical trace (shaded area in **B**) is expanded. Spontaneous fluorescence spikes were clearly detected (small vertical bars), and the shortest interval between fAPs was 17 ms (arrow). The optical trace was filtered with a 50 Hz Butterworth low-pass filter.

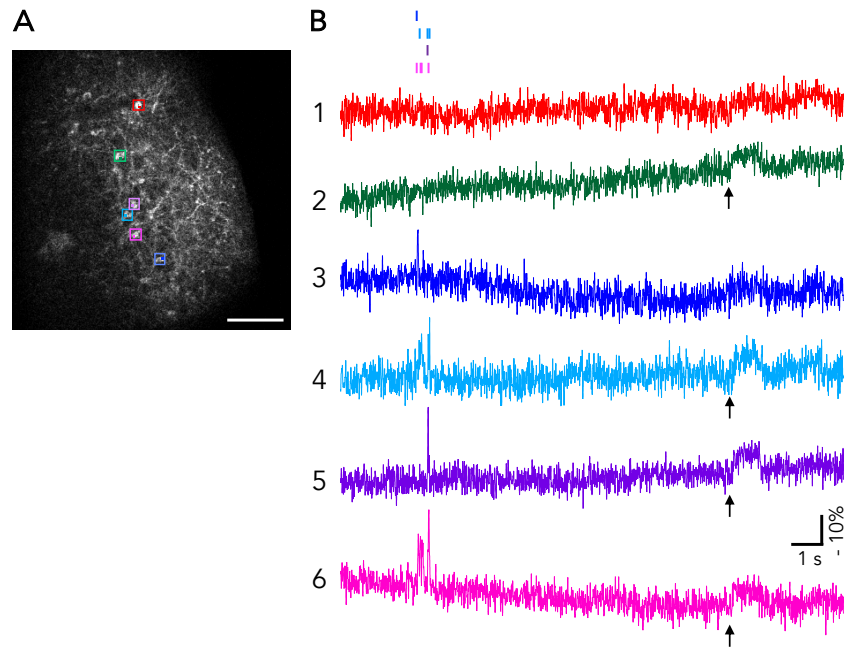


**Figure S6.** Simultaneous voltage measurement in 6 neurons. Related to Figure 4.

- (A)** Two-photon image of a slice. Six neurons in this focal plane (colored boxes) that have strong ASAP3 expression were recorded simultaneously. Scale bar: 100  $\mu\text{m}$ .
- (B)** Color-matched optical traces recorded from the six neurons in **A**. Color bars on the top indicate detected spikes in the color matched traces. The 6 traces share synchronized activities in some parts but independent in other parts, indicating that the signal changes are not reflecting noise. In particular, trace 1 is relatively silent; traces 3/4/6 and traces 4/5/6 have synchronized fAPs; and traces 2/4/5/6 show synchronized baseline changes (arrow). SNR of neurons #3-6 were 4.7, 5.3, 5.4 and 5.3, respectively.

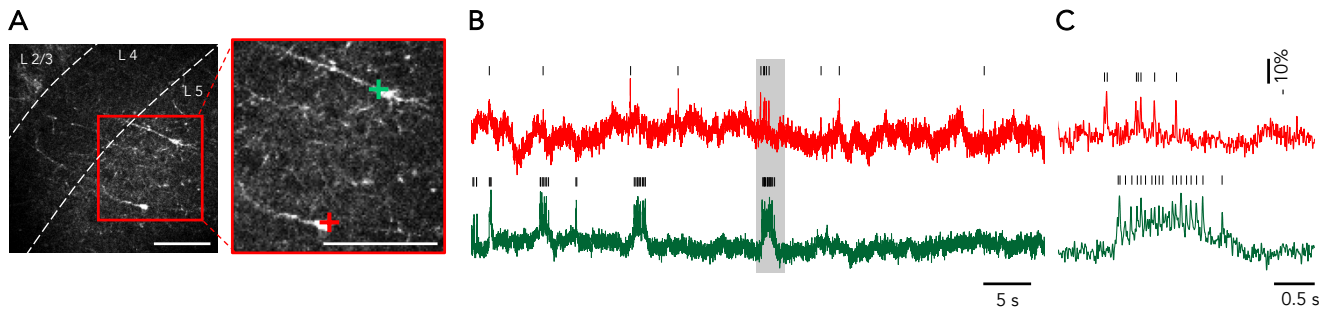


**Figure S7.** Voltage recording from L5 cells. Related to Figure 4.

- (A)** ASAP3 expressed in L5 neurons with IUE at E13.5 The area in the red box in the top image is enlarged in the bottom image. Crosses indicate recording points. Scale bar: 100  $\mu\text{m}$ .
- (B)** AIR recording from the neurons shown in **A**. SNR of the red and green traces were 6.8 and 7.2, respectively. The two neurons exhibit unsynchronized spikes.
- (C)** Expanded traces of the shaded areas in **B**.

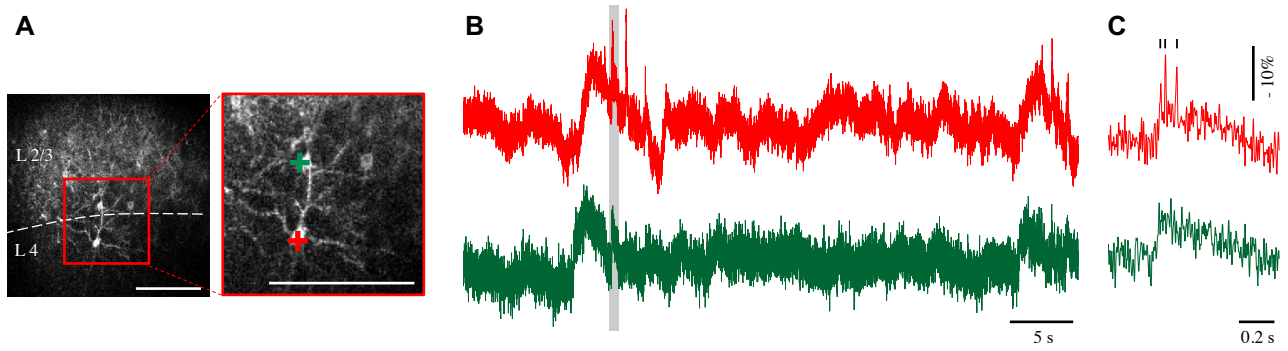


**Figure S8.** AIR recording of interlaminar neuronal activity from L2/3 and L4 cells. Related to Figure 4.

- (A)** ASAP3 expressed in L4 and L2/3 neurons with IUE at E14.5. The boxed area is expanded (right), showing the target pyramidal neurons in L2/3 (green) and L4 (red). Recording points are indicated by crosses. Scale bar: 100  $\mu\text{m}$ .
- (B)** Voltage recording from the neurons shown in **A**. SNR of the red trace was 6.0. The green trace had no detected spikes.
- (C)** Expanded traces of the shaded areas in **B**.

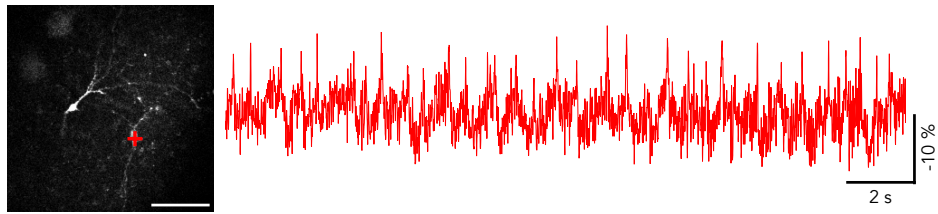


**Figure S9.** AIR recording in hippocampus. Related to Figure 4.

IUE was performed at E14.5 by targeting hippocampus, and hippocampal slices were prepared at P20. Two pyramidal neurons were identified by the shape and location. Multiple optical spikes were observed in one of them (red cross and trace, SNR = 4.9). Scale bar: 100  $\mu\text{m}$ .

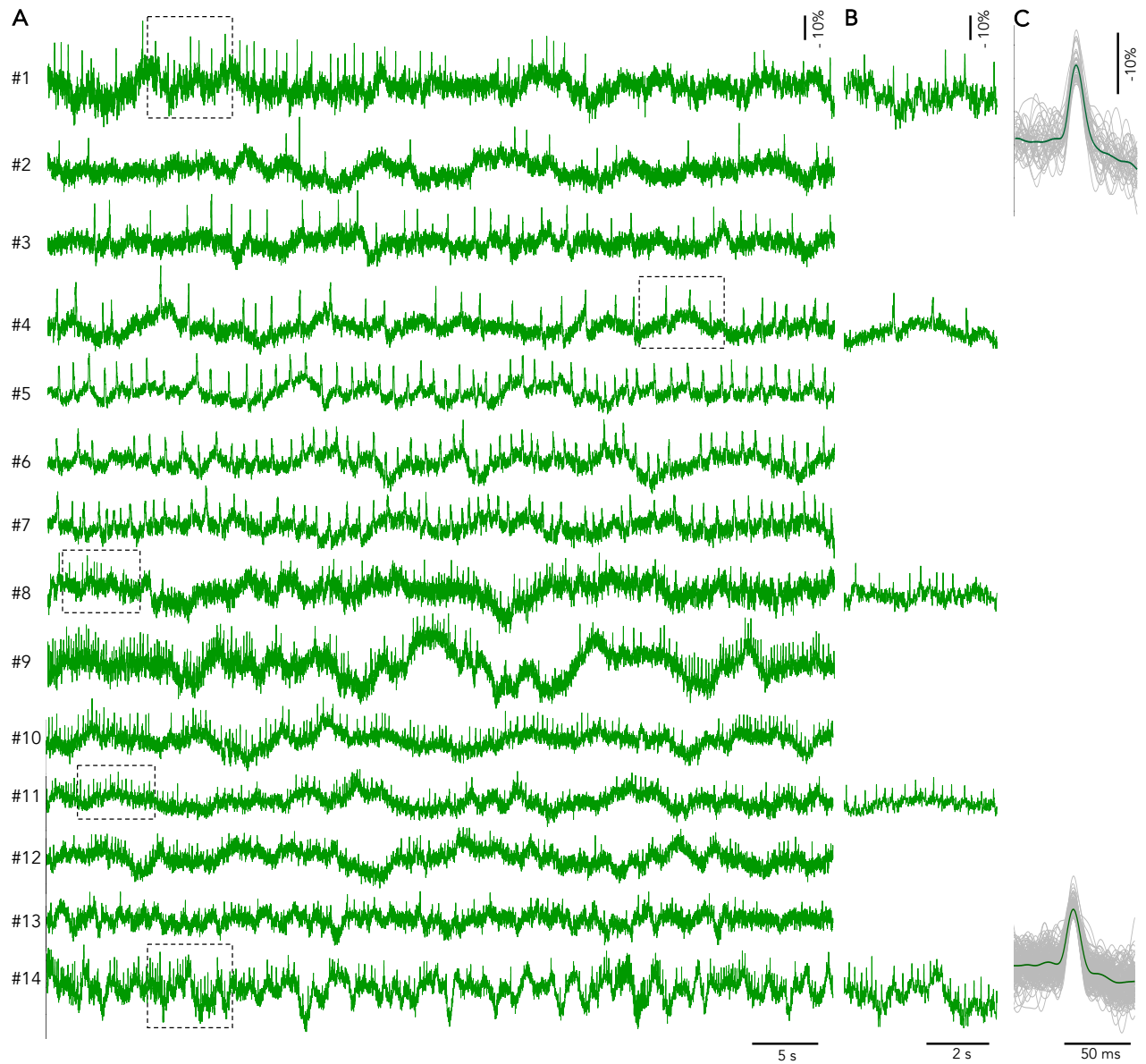


**Figure S10.** Full recording of Figure 5.

- (A)** Optical traces of AIR recording show the total 14 min recording. Optical spikes are clearly distinguishable in every minute of recording. The #1 and #14 min traces are the same traces shown in Figure 5B.
- (B)** Framed areas in **A** are expanded.
- (C)** Averaged waveforms of fAP (green) at the 1st and 14th minute of recording, respectively. Gray traces indicate the individual fAPs.

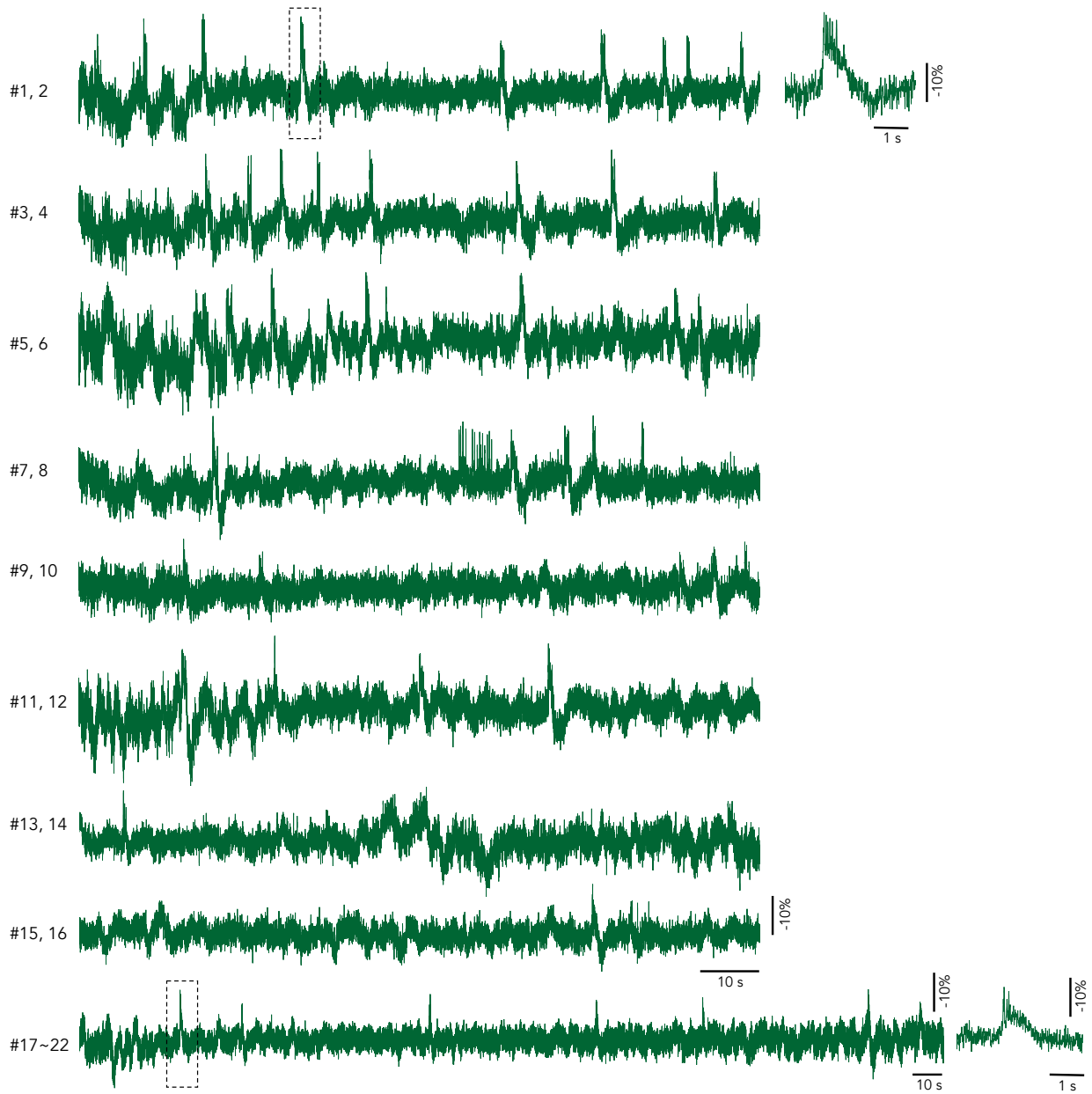


**Figure S11.** An example of long duration recording. Related to Figures 4 and 5.

Full optical traces of a 22 min recording obtained in the green cell in Figure 4. The optical traces were taken every 2 min. The #7, 8 min trace is the same data shown in Figure 4B. Framed area in #1,2 and #17~22 min traces are expanded at the right side.

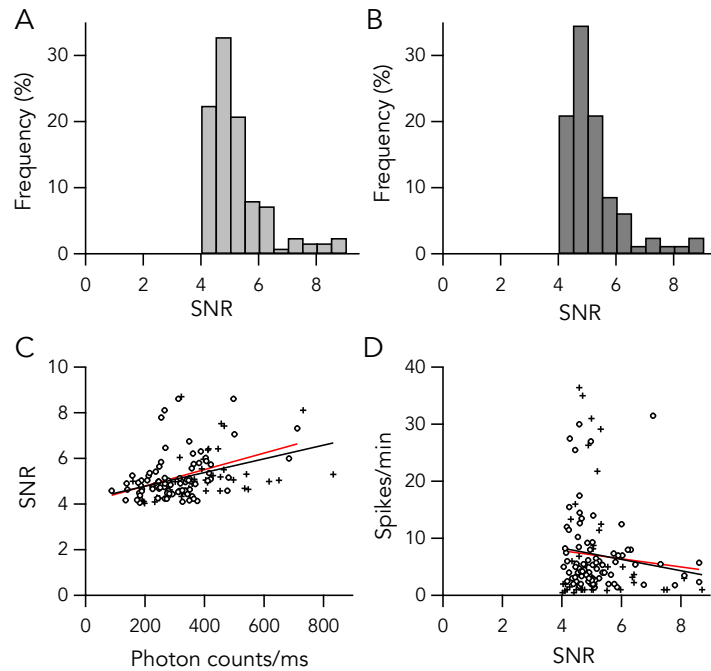


**Figure S12.** SNR of optical recording traces. Related to Figures 7 and 8.

- (A)** Histogram of SNR of all recorded neurons ( $5.2 \pm 1.0$ , mean  $\pm$  SD;  $n = 125$  cells). Since spike was identified by the Schmitt trigger method where events exceeded 4 times larger than SD of the data were picked (see Transparent Method), SNR of all data traces are larger than 4.
- (B)** Histogram of SNR of neurons analyzed in Figures 7 and 8 ( $5.2 \pm 1.0$ ;  $n = 81$  cells).
- (C)** Signal intensity (photon counts per millisecond) and SNR of each neuron are plotted. Circles represent cells analyzed in Figures 7 and 8 ( $n = 81$  cells), and crosses represent other cells ( $n = 44$ ). Signal intensity and SNR have significant correlation in the both data sets (cells analyzed in Figures 7 and 8:  $P < 0.001$  in Pearson's correlation test and  $P < 0.01$  in Spearman's rank correlation test; all cells:  $P < 0.0001$  in the both tests).
- (D)** SNR and number of detected spikes of each neuron are plotted. Marks and lines represent the same data sets and linear regressions as in C. Linear regressions for cells used in Figures 7 and 8 (red) and all cells (black) are shown. SNRs and spike counts have no significant correlation in the both data sets ( $P > 0.05$  in both Pearson's correlation test and Spearman's rank correlation test).

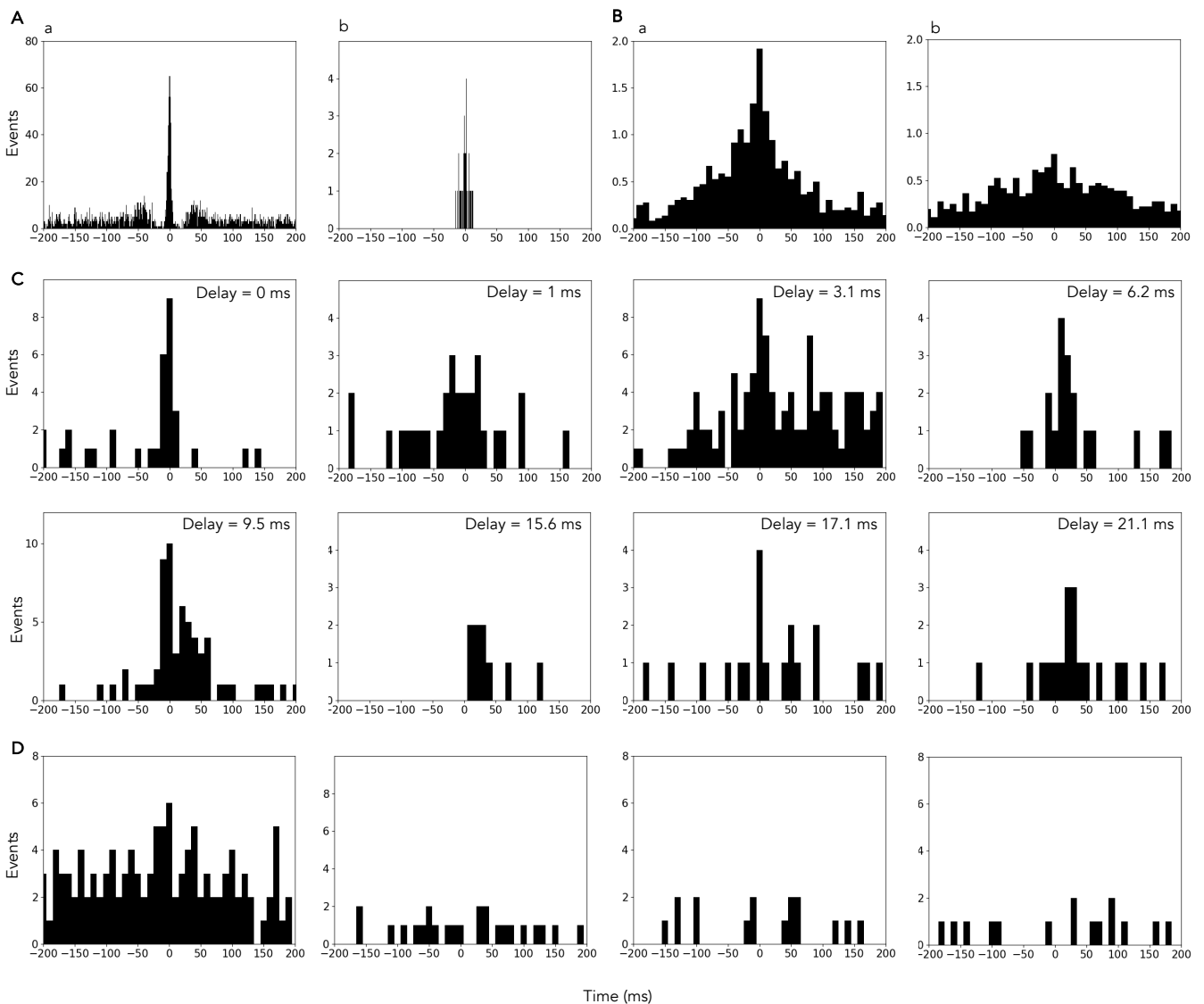


**Figure S13.** Representative cross-correlograms (CCGs). Related to Figure 7.

- (A)** Representative CCGs of spike train pairs recorded at different points of single cells. (a) Recorded at two points in the same cell body. (b) Recorded at soma and dendrite of the same neuron (the neuron shown in Figure 3A-B). Binning width: 1 ms.
- (B)** Average of CCGs of correlated (a,  $n = 46$ ) and uncorrelated (b,  $n = 60$ ) neuron pairs judged by Jitter-based analysis. A narrow peak is identified at 0 ms in a but not in b. Binning width: 10 ms.
- (C)** Representative CCGs of neuron pairs that were judged as correlated by Jitter-based analysis. Delay calculated by the Jitter-based method (shown in Figure 7C) is indicated in each CCG. The neuron pairs of the first and third CCGs are shown in Figure 4, pair 1-2 and pair 2-3, respectively. Binning width: 10 ms.
- (D)** Representative CCGs of neuron pairs that were judged as not correlated by Jitter-based analysis. The neuron pairs of the first and second CCGs are shown in Figure S7 and pair 1-4 in Figure 6, respectively. Binning width: 10 ms.

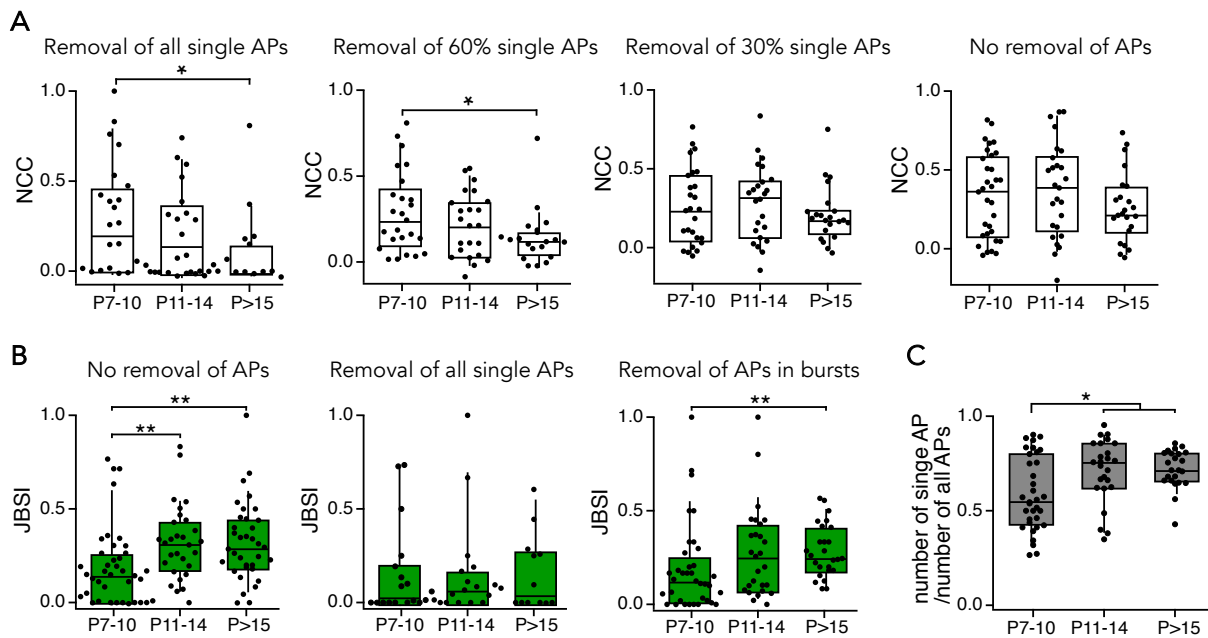


**Figure S14.** Emulation of neuron connection analysis with calcium imaging by thinning out single spikes. Related to Figure 8.

- (A)** Normalized correlation coefficient (NCC) of spike events of neuron pairs were calculated from the same data set used in Figure 6A after thinning out all, 60%, 30%, or 0% of the single spikes. In the data sets in which all and 60% of single spikes were removed, the strength of pairwise neuron connection showed decrease along development.
- (B)** To compare with the NCC analysis method, jitter-based analysis was performed on the same data set without removal of single spikes (left), after removal of all single spikes (middle), or removal of all spikes in bursts (right). The analysis in **B**, left is essentially the same as the left panel of Figure 8A but with a different age classification. The "no removal" and "removal of spikes in bursts" data sets showed increase in the strength of pairwise connection along development.
- (C)** Ratio of number of single APs to that of all APs in different stages. Black dots represent pairs of neurons. Box plots in **A–C** show IQR, range (10–90%), and median. \*:  $p < 0.1$ ; \*\*:  $p < 0.01$ , Mann-Whitney U-test.

## Transparent Methods

### *Animals*

Pregnant ICR mice were purchased from Japan SLC, Inc. (Hamamatsu, Japan). The day of vaginal plug observation was designated as E0.5. The day of birth was designated as P0. All animal experiments were performed under the control of the Institutional Animal Care and Use Committee of Waseda University. The experimental protocols for the animal experiments was approved by the Committee on the Ethics of Animal Experiments of Waseda University.

### *Plasmid*

The pCAG-ASAP3b plasmid (Villette et al., 2019) was purified using an endotoxin-free plasmid purification kit (NucleoBond Xtra Maxi EF, Mancherey-nagel, Düren, Germany) according to the manufacturer's protocol. The purified plasmid was diluted with HEPES-buffered saline (HBS, in mM, 20 HEPES, 115 NaCl, 5.4 KCl, 1 MgCl<sub>2</sub>, 2 CaCl<sub>2</sub>, 10 glucose, pH 7.4) to a final concentration of 4–6 µg/µl, and Fast Green solution (Sigma-Aldrich, Tokyo, Japan) was added at 0.01% to the solution to monitor the injection (Tabata and Nakajima, 2001).

### *IUE*

IUE was performed at E13.5 to E15.5 for ASAP3 expression depending on the targeted brain region. Briefly, pregnant mice were deeply anesthetized by an intraperitoneal injection of sodium pentobarbital (Kyoritsu Seiyaku Corp., Tokyo, Japan) at 50 µg per gram of body weight. After the midline incision was made in abdominal skin and wall, one uterine horn was carefully drawn out. Plasmid solution (1–2 µl) was injected into the lateral ventricle of the intrauterine embryos, and then electric pulses (33–35 V, 50 ms, 4 times) were delivered using an electroporator (CUY21, Nepa Gene, Chiba, Japan) with a forceps-type electrode (CUY650P5, Nepa Gene). To introduce the DNA into a larger region of somatosensory cortex, the anode was placed on the injection site and the cathode was placed on the chin. To introduce the DNA into hippocampus, the IUE was performed at E14.5 and the anode was placed on the opposite side of the injected ventricle (Navarro-Quiroga et al., 2007; Pacary et al., 2012). After that, the uterine horn was returned to the abdominal cavity, and the same procedure was performed on uterine horn. Finally, the abdominal cavity was closed with sutures to allow the embryos to continue normal development.

Positive pups can be screened at P0. In positive pups, green fluorescence in one side of somatosensory cortex can be visible by strong blue light through yellow goggles. After practices, about 90% pups survived after delivery, and the plasmid was successfully transfected into about 90% brains with strong expression.

### *Brain slice*

The ASAP3-transfected mice were sacrificed at P7-P21 for slicing. Brains were sectioned coronally at 400 µm thickness in cooled cutting solution containing (in mM): 120 Choline-Cl, 26 NaHCO<sub>3</sub>, 8 MgCl<sub>2</sub>, 3 KCl, 1.25 NaH<sub>2</sub>PO<sub>4</sub>, and 20 glucose with a vibratome-type slicer (LinearSlicer Pro 7, Dosaka EM, Kyoto, Japan), and left to recover in low-K<sup>+</sup>-type artificial cerebrospinal fluid (ACSF, containing (in mM): NaCl 125, KCl 2.5, NaH<sub>2</sub>PO<sub>4</sub> 1.25, NaHCO<sub>3</sub> 26, MgCl<sub>2</sub> 1, CaCl<sub>2</sub> 2 and glucose 20, 310–315 mOsm, equilibrated with 95% O<sub>2</sub>/5% CO<sub>2</sub>) at room temperature (RT; 20–22°C) for at least 1 h before transfer to a recording chamber. The slices were recorded within 5 hours after recovery. During recording, high-K<sup>+</sup>-type ACSF (difference from the low-K<sup>+</sup>-type ACSF was 122.5 mM NaCl and 5 mM KCl) was used instead, of which K<sup>+</sup> concentration is also popular in brain slice experiments.

### *Design and components of RAMP*

A custom-built random-access two-photon microscope was used to perform voltage recording as described (Shafeghat et al., 2016). The RAMP was built based on the previous design (Salomé et al., 2006). In brief, a femtosecond pulsed Ti:Sapphire laser (output = 600–700 mW,  $\Delta\lambda$  = 10–12 nm, repetition rate = 80 MHz, Tsunami, Spectra Physics Japan, Tokyo, Japan) was pumped by a green laser diode (532 nm, 7.8 mW, SHG-40, Millennia, Spectra Physics Japan) and tuned at 900 nm. The laser beam passed through an acousto-optic modulator (AOM; MTS144-B47A15, AA Opto-Electronic, Orsay, Franc) to pre-compensate for spatial distortions introduced by the AODs, and then deflected by two orthogonal AODs (DTSXY-400-850.950, AA Opto-Electronic) to rapidly and

randomly scan the field of view. The laser beam was passed through selectable high or low magnification light paths by switching the light path with a step motor and two flippers (high: 104×104 μm, low: 415×415 μm). Then, the laser beam was focused on the sample using a 20× 1.0-N.A. water-immersion objective (XLUMPlan FL, Olympus, Tokyo, Japan) mounted on an upright microscope (BX51WI, Olympus). After passing through a 500–550nm band-pass filter (Asahi Spectra, Tokyo, Japan), emitted photons were collected by photomultiplier tubes (H7422PA-40, Hamamatsu Photonics, Hamamatsu, Japan) in the photon-counting mode, which is beneficial in rejecting the majority of photon noise. The time to move the laser beam between voxels in the field of view was 11.5 μs, regardless of the distance between the voxels. When setting the sampling rate at X Hz and number of recording points at Y, the dwell time (d) for each recording point is:

$$d = \frac{1 \times 10^6}{X \times Y} - 11.5 \mu s$$

The sampling rate was set to 2–10 kHz. Estimated dimensions of laser spot was 3 μm for the axial axis with radius of 0.35/1.4 μm for high/low magnification (Heidarinejad et al., 2018). All devices were controlled by TI Workbench, a custom-made software written by T.I. (Inoue, 2018).

### Voltage imaging with RAMP

Acute cerebral slices were visualized in a chamber continuously superfused with the high-K<sup>+</sup>-type ACSF at RT under the two-photon microscope. ASAP3 expressing neurons were identified by two-photon excitation, and voltage recording was performed on bright neurons in the somatosensory cortex. In each neuron, recording points were chosen among bright points on the plasma membrane. Before starting the recording, ACSF was warmed to 33–35°C as ASAP3 has approximately 4-fold faster kinetics at 33–35°C than at RT (Villette et al., 2019). For multi-cell recording, voltage recording was performed at 2 kHz with the low magnification light path. When recording spike propagation within neurons, voltage recording was performed at 10 kHz with the high magnification light path to increase spatiotemporal resolution. All devices were controlled and data were acquired with the TI Workbench software running on a Mac computer (Inoue, 2018).

### Data analysis

**Analysis of spike trains.** For each optical trace, high-frequency noise was removed by low-pass Butterworth filter, and periods with shaky baseline were discarded. Then, APs were detected as fluorescence spikes in TI Workbench using a Schmitt trigger method (Shafeghat et al., 2016). The time series of low-pass filtered raw fluorescence intensity,  $F_{raw}(i)$ , had baseline drift (see Figure 1C) due to photobleaching, tissue movement and other causes, which was corrected by calculating baseline by linear regression with a 100 ms temporal window just before each data point,  $F_{base}(i)$ . Time series of corrected fluorescence intensity change for each point,  $\Delta F(i)$ , was calculated as:  $\Delta F(i) = -[F_{raw}(i) - F_{base}(i)]$ .  $\Delta F$  is positive in depolarization. If  $\Delta F$  exceeded 4 times of standard deviation (SD) of the entire baseline-corrected data points and kept exceeding SD for more than 2 ms, this data range was determined as a spike event (fAP) with peak amplitude and peak time as the maximum  $\Delta F$  value within the period and time of the maximum  $\Delta F$ , respectively. Noise level was defined as  $SD/F_{base}(i)$ , and SNR was calculated as  $SNR(i) = \Delta F(i)/SD$ .

**Spike timing accuracy.** To determine the spike timing accuracy of the optical recording, fluorescence signals were recorded at two locations (A and B) of the same soma simultaneously (Figure S3). And the spike timing accuracy were determined as the peak time differential between the synchronized spikes recorded from the two locations ( $|Ta_i - Tb_i|$ , where  $Ta_i$  is the spike timing of the #i spike occurred in trace A, and  $Tb_i$  is similar to  $Ta_i$ ).

**Jitter-based analysis.** Pairwise correlation of neuron pairs was evaluated by a jitter-based synchrony analysis (Agmon, 2012). In particular, Jitter-based Z-score was calculated from each pair of spike trains derived from multi-cell recordings of spontaneous activity, determining whether the pair of neurons fired independently and the apparent synchrony was therefore happened by chance (null hypothesis), or the neurons were coupled by synaptic connection or by a common input from a third neuron (functionally connected). The Jitter-based Z-score was calculated as:

$$Z = \frac{N_c - \langle N_c^J \rangle}{\sqrt{Var(N_c^J)}}$$

$N_C$  is the number of spike coincidences within a synchrony span,  $\tau_s$ . It can be represented graphically as the number of spikes in slower firing neuron that fall within a synchrony window centered on each spike in faster firing neuron with  $2\tau_s$  width.  $\langle N_C^J \rangle$  is the expected value of the number of spike coincidences after shifting each spike in the lower firing cell within the jitter span,  $\tau_j$ . Graphically, jitter windows are drawn centered on each spike in slower firing neuron with width  $2\tau_j$ . The overlap probability  $p_i$  is defined as the overlap fraction of its jitter window (blue window). And  $\langle N_C^J \rangle$  is the sum of  $p_i$  (see Figure 1 of Agmon, 2012). And  $Var(N_C^J)$  is the variance of the number of spike coincidence after applying the jitter, which can be calculated as  $\sum_i p_i \times (1 - p_i)$ .

To quantify correlation strength, jitter-based synchrony index (JBSI) was calculated as:

$$JBSI = \beta \frac{N_C - \langle N_C^J \rangle}{n_1}$$

where  $n_1$  is the number of spikes in the lower firing cell of the pair.  $\beta = 2$  when  $\tau_s/\tau_j \leq 2$ , and  $\beta = \tau_j/(\tau_j - \tau_s)$  when  $\tau_j/\tau_s > 2$ . We chose  $\tau_j/\tau_s$  to be 2 for simple calculation. Thus,  $\beta = 2$  in our analysis. Neurons showing less than 6 spikes during the entire recording period were discarded. As JBSI is a well normalized synchrony index, which is independent of firing rate, not sensitive to the firing rate difference of neuron pair and not requiring specific firing patterns, it allows valid comparison of correlation strength of neuron pairs obtained from different experiments. JBSI = 1, -1 and 0 indicate perfect positivity synchrony, perfect negative synchrony, and chance-level synchrony, respectively.

Both Z-score and JBSI depend on  $\tau_s$ . The slope of JBSI versus  $\tau_s$  curve is gentle on the right of the peak and steep on the left. JBSI has a maximum value when  $\tau_s$  equals to the temporal precision of fAPs, which depends on the lag of spike pairs together with the temporal error in peak detection (see Figure 3 of Agmon, 2012). Thus, the points at which the JBSI -  $\tau_s$  curve drops off steeply to the left should be used as cutoff  $\tau_s$  for determining spike lag and JBSI calculation. As different neuron pairs may have different spike lags, neuron pairs have their maximum JBSI values (JBSI<sub>max</sub>) with different cutoff  $\tau_s$ . JBSI values were calculated while  $\tau_s$  was changed from 1 to 100 ms with a 1 ms step, and the maximum value was determined as JBSI<sub>max</sub> and corresponding  $\tau_s$  was used as cutoff  $\tau_s$  for each neuron pair. And the  $\tau_s$  value was also used to calculate Z-score. Neuron pairs with  $Z > 1.96$  (corresponding to  $p < 0.05$  for a two-tailed Z-test) were considered to have statistically significant connection. Comparing with fixed  $\tau_s$ , using shifted  $\tau_s$  did not affect the evaluation of significance. We tested it by: 1) generation of two completely random artificial spike trains (theoretically, the two trains have no significant correlation); 2) calculation of their significance of correlation; 3) repeat of the 1&2 steps for hundreds of times and evaluation of the false-positive rate. When using the shifted  $\tau_s$ , false-positive happened 3 times after 500 times repeat, which we consider acceptable. And when using a fixed  $\tau_s$  (fixed at 100 ms), false-positive cases were also 3 times in 500 tests. Thus, using shifted  $\tau_s$  seemed to have no obvious influence on the evaluation compared with using fixed  $\tau_s$ , and the false-positive rates for the both were acceptable.

And the value of cutoff  $\tau_s$  was used for quantification of correlation lag. Neuron pairs that had more than 6 synchronous spikes were used for analysis of correlation lag.

**NCC analysis.** To emulate pairwise correlation analysis with calcium imaging, we applied normalized correlation coefficient (NCC) analysis (Golshani et al., 2009; Tchumatchenko et al., 2011) to the spike time series data set obtained in this study. Before NCC analysis, all or part of single spikes were thinned out from spike time series of each neuron, then were binned with 1 s intervals. fAPs with less than 300 ms interval with nearby fAPs were defined as APs in bursts, and other APs were defined as single spikes. NCC of each pair of processed spike time series was calculated using the formula:

$$NCC = \frac{CC}{\sqrt{AC1 \times AC2}}$$

where CC is the cross-correlation coefficient of the spike time series pair (trace 1 and 2), and AC1 and AC2 are the autocorrelation of time series 1 and 2. When part of single spikes were thinned out, predetermined number of single spikes were randomly chosen and NCC was calculated after removal of the chosen single APs. This random selection and NCC calculation were performed 100 times and average of the NCC values was obtained. Neurons showing less than 6 spikes during the entire recording period were discarded.

**Statistics.** Data following a normal distribution were represented as means  $\pm$  SD with bar plots. When normal distribution cannot be assumed, results were represented as median and IQR [25th and 75th percentile] with box

plots. Before performing statistical comparisons, the Shapiro-Wilk method was used to test whether the data followed a normal distribution. If so, statistical comparisons between two data sets were performed with two-tailed paired or independent-samples Student's t-test if the two groups had equal variance. When equal variance cannot be assumed, Welch's t-test was used. If the data do not follow normal distribution, Mann-Whitney U nonparametric test was performed. Statistical correlation between two data sets was calculated with both Pearson's correlation test and Spearman's rank correlation test. Statistical tests were performed in Excel (Microsoft) or Igor Pro (WaveMetrics, Portland, OR, USA). JBSI and NCC were computed with custom Python scripts.

**Figure display.** For display in the figures, fluorescence intensity traces were filtered and corrected for photobleaching and normalized to baseline using Igor Pro. The procedures were shown in Figure 1C. First, the raw traces (Figure 1C top, lighter traces) were filtered with 50 Hz Butterworth low-pass filter (Figure 1C top, darker traces show the filtered data). Then, the filtered traces were fitted with a double or single exponential function (Figure 1C, top, black traces). Optical traces with initial rapid photobleaching were fitted well with a double exponential function (e.g. the pink trace), and slow photobleaching traces were fitted well with a single exponential function (e.g. the green trace). Finally, the filtered optical traces were corrected for photobleaching and normalized by dividing the traces by the fit function (Figure 1C, bottom).

## Supplemental References

- Heidarinejad, M., Nakamura, H., and Inoue, T. (2018). Stimulation-induced changes in diffusion and structure of calmodulin and calmodulin-dependent protein kinase II proteins in neurons. *Neurosci. Res.* 136, 13–32.
- Inoue, T. (2018). TI Workbench, an integrated software package for electrophysiology and imaging. *Microscopy* 67, 129–143.
- Pacary, E., Haas, M.A., Wildner, H., Azzarelli, R., Bell, D.M., Abrous, D.N., and Guillemot, F. (2012). Visualization and genetic manipulation of dendrites and spines in the mouse cerebral cortex and hippocampus using in utero electroporation. *J. Vis. Exp. JoVE* 65, 4163.
- Shafeghat, N., Heidarinejad, M., Murata, N., Nakamura, H., and Inoue, T. (2016). Optical detection of neuron connectivity by random access two-photon microscopy. *J. Neurosci. Methods* 263, 48–56.
- Tabata, H., and Nakajima, K. (2001). Efficient in utero gene transfer system to the developing mouse brain using electroporation: visualization of neuronal migration in the developing cortex. *Neuroscience* 103, 865–872.